

Characterization of Five-Hole Probes used for Flow Measurement in Stack Emission Testing

Iosif Shinder¹, Aaron Johnson, Michael Moldover, James Filla, Vladimir Khromchenko
Sensor Science Division, NIST, Gaithersburg, MD 20899

NOMENCLATURE

Variables with Roman Letters

$a_{q,0}$ - zeroth degree polynomial fit coefficient of null data (equals Γ_{NULL}^q)

c_0, c_1, c_2 - fit coefficients for density correlation

C_{LDA} - calibration coefficient for NIST's Laser Doppler Anemometry (LDA) system (Usually $C_{LDA} = 1.$)

$F_1 = \Delta P_{45, NULL} / \Delta P_{12, NULL}$ - pitch calibration factor

$F_2 = \sqrt{\rho V_{LDA}^2 / 2 \Delta P_{12, NULL}}$ - velocity calibration factor

\vec{n}_{p1} - unit vector normal to port 1 on five-hole probe

T - static temperature of the air in the wind tunnel

P - static pressure of the air in the wind tunnel

P_{offset} - yaw pressure at which null parameters are measured (may be offset from zero)

RH - relative humidity of the air in wind tunnel

$PR_1 = \Delta P_{45} / \Delta P_{12}$ - Pitch pressure ratio

$PR_2 = \sqrt{\Delta P_{dyn} / \Delta P_{12}}$ - Velocity pressure ratio

$r(x_m, x_n)$ - normalized correlation coefficient between variables x_m and x_n

$u(x)$ - uncertainty of input quantity x at the 68 % confidence level

$u_{c,p}(y)$ - combined propagated uncertainty of measurand y at the 68 % confidence level

$u_{c,np}(y)$ - combined non-propagated uncertainty of measurand y at the 68 % confidence level

$u_c(y)$ - combined uncertainty of measurand y at the 68 % confidence level

$U(y)$ - expanded uncertainty of measurand y at the 95 % confidence level

V_{LDA} - airspeed measured by NIST's Laser Doppler Anemometry (LDA) working standard

V_{PITOT} - airspeed measured by NIST's standard L-type pitot probe check standard

V_z' - local velocity along stack axis

Variables with Greek letters

α - pitch angle measured by traverse system

Γ_q - global probe variable equals a null parameter or calibration coefficient depending on value of q

$\Delta P_{dyn} = \rho V_{LDA}^2 / 2$ - dynamic pressure based on air density and airspeed

¹ Corresponding Author: iosif.shinder@nist.gov

$\Delta P_{mn} = P_m - P_n$ - measured differential pressure across ports “m” and “n” of the five-hole

- $\Delta P_{45} = P_4 - P_5$ - *pitch pressure*
- $\Delta P_{23} = P_2 - P_3$ - *yaw pressure*
- $\Delta P_{12} = P_1 - P_2$ - *velocity pressure*

ΔP_{zero} - zero reading of differential pressure transducer

ΔP_{cal} - differential pressure reading within calibrated range transducer

ε - positive number much less than 1

ρ - air density

θ - yaw angle measured by traverse system

Ψ - rational polynomial curve fit of calibration data

Subscripts

ALIGN - alignment of yaw angle or pitch angle during probe installation

EOS - Equation of State

FIT - curve fitted value

LDA - Laser Doppler Anemometry

NULL- condition where yaw pressure is zero ($\Delta P_{23} = 0$)

q - global probe parameter with values 1, 2, 3, 4, or 5

r - relative value

TRAV - wind tunnel traversing system

x – axis of wind tunnel

ABSTRACT

We report progress towards the goal of reducing the errors in industrial smokestack flow measurements to 1 % by replacing S-probes with calibrated 3-D probes (i.e., probes that measure 3 components of velocity). NIST calibrated a commercially-manufactured spherical probe and a prism probe at air speeds (5 m/s to 30 m/s) and pitch angles (-20° to 20°) using a yaw-nulling method similar to EPA's Method 2F. The expanded uncertainty for 3-D air speed measurements of both probes was near 1 % at a 95 % confidence level. Most of this uncertainty is attributed to the reproducibility of the calibration measurements and the uncertainty of the NIST's laser doppler anemometer air-speed standard. Thus, the 1 % goal might be possible; however, to obtain this low uncertainty, two significant uncertainties consistent with EPA Method 2F must be avoided. First, the Reynolds number dependence of the prism probe must be accounted for during probe calibration, and second, more stringent uncertainty requirements are needed for the yaw-pressure measurement at low flows.

1 INTRODUCTION

Accurate stack-flow measurements are required to measure hazardous emissions from industrial smokestacks. Today, most stack flow measurements use an S-type pitot probe (or S-probe), which measure only two components of the flow velocity. When the velocity field in stacks is highly 3-dimensional, S-probe surveys can have errors of 10 % or more [1 – 4]. Here, we report progress towards the goal of reducing stack flow survey errors to 1 % by replacing S-probes with calibrated probes that measure 3 components of velocity.

The U.S. Environmental Protection Agency (EPA) has developed regulations supporting two types of commercially available 3-D probes including a 5-hole prism probe and a 5-hole spherical probe shown in Figures 1A and 1B. These probes are calibrated and used in accordance with EPA document Method 2F [5]. The protocols in Method 2F stipulate 1) the design features of the wind tunnel used to calibrate probes (e.g., minimum cross section dimensions, flow stability, range of air speeds, maximum level of off-axis flow), 2) the calibration procedure to determine the Method 2F calibration factors, aptly named F_1 and F_2 , 3) the procedure for using the probe to measure the volumetric flow in industrial stacks, and 4) the uncertainty specifications of auxiliary measurements of differential pressure, yaw angle, and pitch angle. However, the uncertainty of the calibration factors F_1 and F_2 are not specified. Therefore, it is not clear what level of uncertainty reduction, if any, will be gained by replacing an inexpensive two-dimensional (2-D) S-probe with a more complex three-dimensional (3-D) probe. If 1 % stack flow measurements are the goal, then the uncertainty of these calibration factors should be no larger than 1 % at the 95 % confidence level.

The National Institute of Standards and Technology (NIST) has experience calibrating both prism probes and spherical probes using nulling and non-nulling methods. For each probe type, the calibration factors have the same general characteristics. In this work we calibrated the prism probe and the spherical probe shown in Figures 1A and 1B using the Method 2F protocol; however, NIST implementation of Method 2F exceeded the protocol's minimum requirements. Several steps were taken to obtain the highest quality data with the lowest possible uncertainty. First, we characterized the probes' Reynolds number (Re) dependence over the full velocity range (5 m/s to 30 m/s) of typical coal-fired power plant stacks. In addition, we evaluated the probe

performance over a wide range of pitch angles ($\alpha = -45^\circ$ to 45°). The calibration was performed in NIST's wind tunnel [1] against the U.S. national standard for wind speed, a laser doppler anemometer (LDA) traceable to the SI unit of velocity *via* length and time [6].

Second, we computed the expanded uncertainties² of the both the pitch calibration factor F_1 and the velocity calibration factor F_2 for both 3-D probes. The results showed the expanded uncertainty (95 % confidence level) of the velocity calibration factor $100 \times U(F_2)/F_2$ ranged from 0.9 % to 1.1 % for the spherical probe and from 0.9 % to 1.25 % for the prism probe for pitch angles $\alpha = -20^\circ$ to 20° . We performed multiple calibrations on each probe and included reproducibility in the uncertainty budget. For both probes reproducibility was a major factor in the uncertainty budget, contributing more than 50 % to the total uncertainty. Given that the uncertainties of these probes have not been documented over the wide range of pitch angles and velocities investigated herein, these results will give the stack flow measurement community the groundwork for computing the uncertainty as well as provide a baseline of the best possible performance once can expect from these devices.

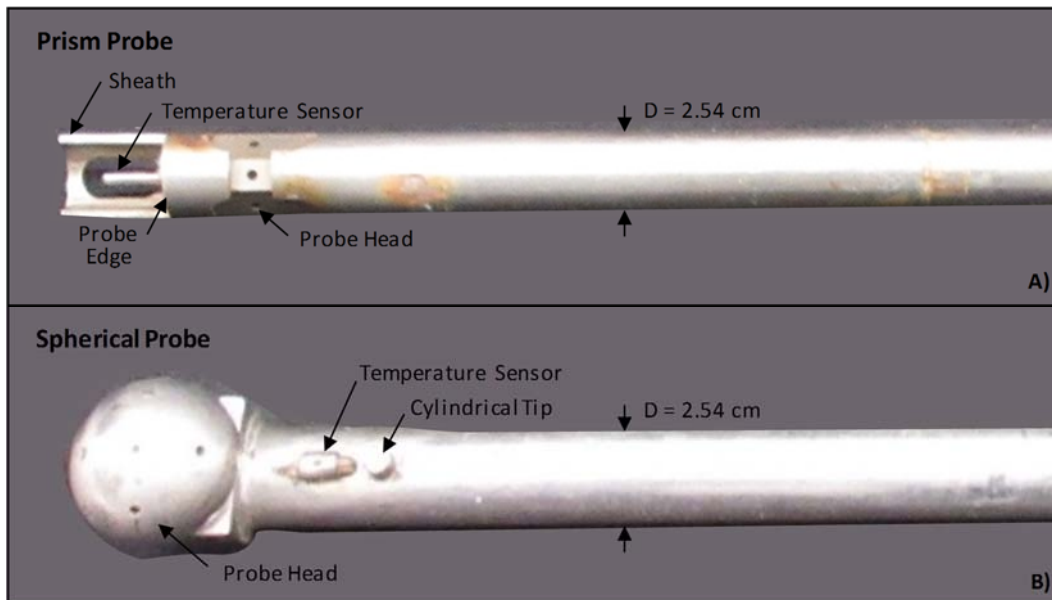


Figure 1. Picture of A) 5-hole prism probe and B) 5-hole spherical probe. The nominal diameter and probe length of each probe was $D = 2.54$ cm (1 inch) and 1.83 m (6 ft).

Third, we developed robust correlations that calculate the probe velocity calibration factor (F_2) and pitch angle (α) as a function of the measured pitch pressure and velocity pressure at the yaw-null angle. The correlation accounts for the probes' Re - dependence and pitch angle response over the range of pitch angles, $F_2 = F_2(\alpha, Re)$. For $\alpha = -20^\circ$ to 20° we found that $F_{2,PRISM}$ had a strong Re -dependence while $F_{2,SPHERICAL}$ was nearly independent of Re . Because the Method 2F protocol allows probes to be calibrated at only two air speeds, 18.3 m/s and 27.4 m/s, the resulting F_1 and F_2 calibration factors are extrapolated to lower velocities during application. This extrapolation procedure works reasonable well for the spherical probe since $F_{2,SPHERICAL}$ is nearly independent of

² Herein the expanded uncertainty is the uncertainty with a confidence interval of 95 % or equivalently with a coverage factor of two ($k = 2$). A capital U is used throughout to denote expanded uncertainty.

Re. A reference value of $F_{2,SPHERICAL}$ measured at 20 m/s deviated less than $\pm 1\%$ with $F_{2,SPHERICAL}$ at other air speeds; the only exception occurred at the lowest air speed of 5 m/s where the deviation increased to nearly 2%. However, for the prism probe the extrapolation introduces a 6% error at low air speeds (< 10 m/s). To accurately measure low velocities a prism probe must be calibrated at low velocities so that the *Re*-dependence of $F_{2,PRISM}$ is adequately characterized.

Finally, we ensured that the accuracy of low speed (< 10 m/s) yaw pressure measurements only made a negligible contribution to the F_1 and F_2 uncertainty budget. When Method 2F protocol is implemented the uncertainty of the yaw pressure measurement can be significant at low speeds for the following 3 reasons. First, Method 2F only requires that the yaw pressure measurement be 1% of full-scale where the full-scale is 124.4 Pa. As such, the accuracy of the yaw pressure measurement can be a significant fraction of the of the dynamic pressure at low air speeds. Second, during a flow RATA, Method 2F allows the differential pressure transducer that measures yaw pressure to drift by as much as 7.5 Pa. At low flue gas velocities, the uncertainty attributed to the zero drift can be a significant fraction of the dynamic pressure, leading to a large uncertainty in the yaw pressure measurement. Finally, Method 2F requires *nulling the probe* or equivalently finding the yaw angle resulting in zero yaw pressure at each traverse point. In practice, finding the probe yaw-angle where the yaw-pressure is zero is difficult due to noisy pressure signals. This is especially true in typical stack applications that have swirling, turbulent flows. Method 2F does not require time-averaging the yaw pressure measurements and adjusting the yaw angle until the actual zero yaw pressure is determined. Consequently, the F_1 and F_2 values determined using Method 2F are generally measured at a yaw-pressure close to, but not exactly equal to zero. This uncertainty has not been documented in Method 2F, but it can be significant at low velocities.

To mitigate the large yaw pressure uncertainties that occur at low velocities we took the following 3 steps. First, we measured the yaw-pressure with a stable, low uncertainty yaw-pressure transducers with uncertainty specifications based on 0.2 percent of reading instead of 1% percent of full-scale. Second, we ensured that zero drift was negligible relative to other uncertainty components during calibration. Finally, we implemented a curve fit method (CFM) to ensure that the calibration factors F_1 and F_2 are determined at a zero yaw-pressure, even when pressure signals are noisy due to flow noise.

This manuscript documents the calibration procedures used by NIST, gives the results for both 3-D probes, and documents their uncertainty calculations. We hope that this paper will guide the stack flow community in estimating the uncertainty of Method 2F calibrations. The low uncertainties obtained herein are generally not obtainable using Method 2F unless certain modifications are made to the protocol. We conclude the manuscript by discussing modifications that should be made to Method 2F to avoid unexpected large uncertainties.

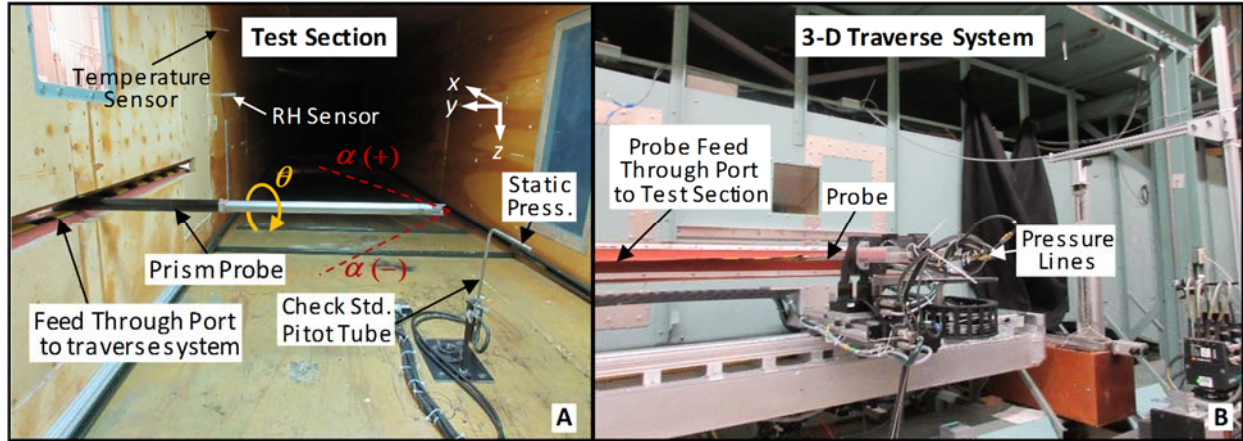


Figure 2. 3-D probe installed in NIST wind tunnel: A) definitions of the pitch (α) and yaw angles (θ), B) NIST 3-D Automated Traverse System. (Note that the air flow moves in the direction of the x-axis in Fig. 2).

2 DESCRIPTION OF NIST'S WIND TUNNEL

Air speed measurements were performed in the 2 m long rectangular test section of our recirculating wind tunnel [7 - 10]. The cross section is 1.2 m high by 1.5 m wide. This large cross-section minimizes the probe-induced blockage effects and the profile effects attributed to the boundary layer along the wall. LDA surveys (without a probe installed) demonstrate a uniform velocity in the test section's measurement zone. Figure 2A shows a 5-hole prism probe installed in the test section. Since the presence of the probe disturbs the velocity field, the LDA velocity (V_{LDA}) is measured in the freestream upstream of the probe's zone of influence.

The velocity measured by the LDA is converted to dynamic pressure by

$$\Delta P_{\text{dyn}} = \frac{\rho V_{LDA}^2}{2} \quad (1)$$

where ρ is the air density in the test section, which is calculated by

$$\rho = \frac{c_0}{T} \left[P - c_1 RH \exp\left(-\frac{c_2}{T}\right) \right] \quad (2)$$

where the coefficients have the following values $c_0 = 3.4848 \times 10^{-3}$ K kg/J, $c_1 = 6.65287 \times 10^8$ Pa, and $c_2 = 5315.56$ K; RH is the relative humidity of the air in percent, P is the static pressure in Pascal, T is air temperature in Kelvin, and the air density is in units of kg/m³. The pressure is measured using the static pressure ports on the NIST check standard pitot probe shown in Fig.2A. The figure also shows the location where the temperature and relative humidity are measured.³ The standard relative uncertainty of density equation of state is $u_{\text{EOS},r}(\rho) = 0.1\%$ [11].⁴ The standard uncertainties of the temperature, pressure, and relative humidity (RH) are $u(T) = 1$ K, $u(P) = 0.1$ kPa, and $u(RH) = 5\%$, respectively. These uncertainties are multiplied by their

³ In Fig. 2 the temperature sensors attached to the probes were not the ones used in this calibration.

⁴ Throughout this manuscript we denote relative uncertainties using the subscript "r", so that $u_r(x) = 100 u(x)/x$ is a dimensionless value expressed as a percent; here, x is the measurand and $u(x)$ is the dimensional standard uncertainty of the measurand at a confidence interval of 68% or equivalently with a coverage factor of unity ($k = 1$).

respective normalized sensitivity coefficients and root-sum-squared to give the relative uncertainty in the computed density.⁵ For the range of air speeds in this calibration (5 m/s to 30 m/s) the expanded uncertainties of the LDA and L-shaped pitot probe are $U_{r,LDA} = 0.41\%$ and $U_{r,L-PITOT} = 0.44\%$ [6], respectively.² During the calibration the average difference between the LDA airspeed (V_{LDA}) and the L-shaped pitot probe air speed (V_{PITOT}) differed by no more than 0.1 %, well within their expected uncertainties.

Probes are oriented to specific pitch angles in the range $-45^\circ \leq \alpha \leq 45^\circ$ and yaw angles in the range $-180^\circ \leq \theta \leq +180^\circ$ by the 3-D traverse system attached to the outside of the wind tunnel shown in Fig. 2B. The probe is installed into the test section through the narrow rectangular slot called the feed-through port. Velocity surveys have shown that air leakage into the test section through the feed through has a negligible effect on air speed measurements, provided the probe is positioned near the center of the wind tunnel. As shown in Fig. 2A the yaw angle (θ) corresponds to rotations about the probe axis while the pitch angle (α) rotates the probe in the x-y plane about the pressure-sensing port 1 (see Fig. 3 for pressure port locations). Consequently, when the traverse system moves the probe to a specified pitch angle the physical location of port 1 in the test section remains unchanged. In addition, the physical location of the LDA velocity measurement coincides with the streamline normal to port 1. The positive yaw angle direction is indicated by the direction of the arrow in Fig. 2A and the positive and negative pitch angles are denoted by the respective positive sign (+) and negative sign (-).

A custom software program controls the air speed and the probe pitch and yaw angle settings. The program also acquires the calibration data including the LDA velocity, the required differential pressure measurements, pitch, yaw, etc. Data acquisition uses several different communication interfaces. Pressure-based instrument readings are acquired using a PCI-based multifunction DAQ board, while auxiliary LabVIEW programs are used to continuously monitor the Laser Doppler Anemometer and environmental sensors (*i.e.*, temperature, pressure, and relative-humidity). The program ensures flow is stable and within $\pm 0.2\%$ of set point velocity during data collection.

5 Section 5.1 gives details for calculating sensitivity coefficients and performing uncertainty analysis.

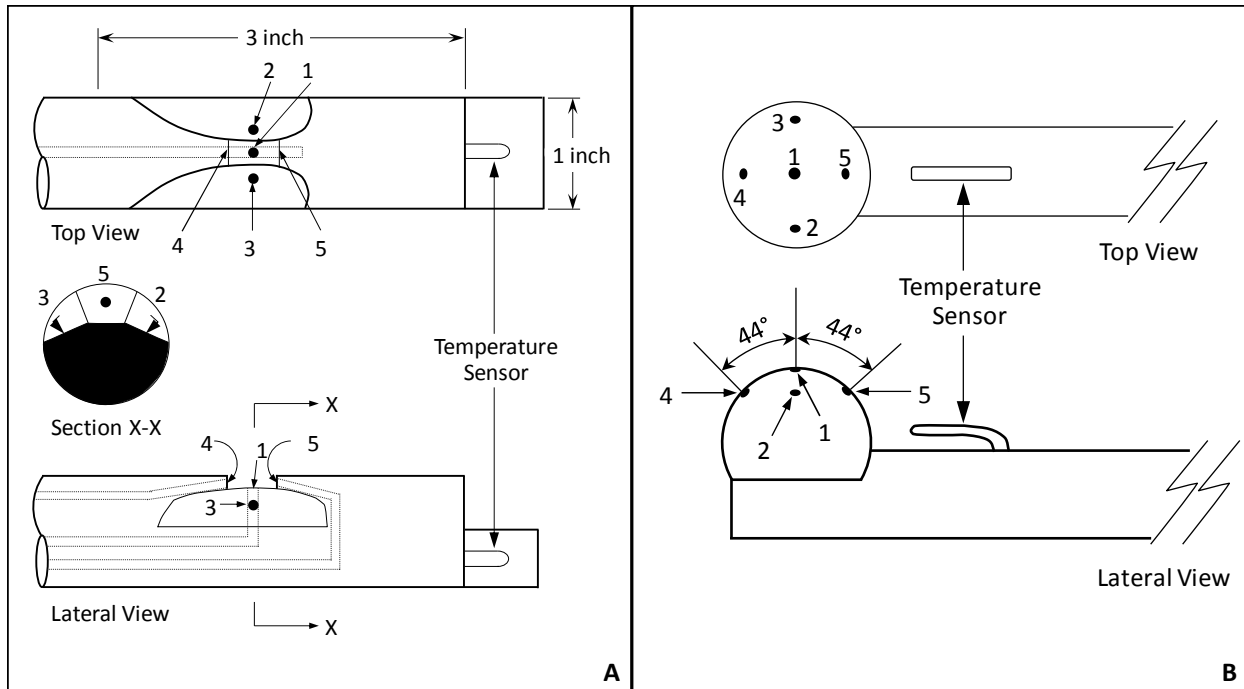


Figure 3. Probe head geometries and port locations 1, 2, 3, 4, and 5 for Prism probe (A) and Spherical probe (B).

3 PROBE DESCRIPTION AND INSTALLATION

3.1 Differential Pressure Measurements

Figures 3A and 3B show the shapes of the prism probe head, the spherical probe head, and the location of the 5 pressure ports on each probe. The pressure ports are labeled 1, 2, 3, 4, and 5. We measured the differential pressures across the ports using four 10 Torr (10 Torr = 1333.22 Pa) model 698A Baratron heated, high accuracy, bidirectional differential capacitance manometers.⁶ For convenience, we define the pressure difference between any two ports by

$$\Delta P_{mn} = P_m - P_n \quad (3)$$

where P_m is the pressure of port “m” where $m = 1, 2, 3, 4,$ or 5 and P_n is the pressure of port “n” where $n = 1, 2, 3, 4,$ or 5 . We connected the four pressure sensors to the pitot probe ports so that the first sensor measured ΔP_{12} ; the second transducer measured ΔP_{13} ; etc. The standard uncertainty of each differential pressure transducer is $u_r(\Delta P_{cal}) = 0.1\%$ of reading for $\Delta P_{cal} = 2$ Pa to 666.7 Pa and from $\Delta P_{cal} = -2$ Pa to -666.7 Pa.⁷ A conservative estimate of the standard uncertainty attributed to zero drift is conservatively taken to be $u(\Delta P_{zero}) = 0.002$ Pa. Thus, the uncertainty of differential pressure measurements is

6 Certain commercial equipment, instruments, or materials are identified in this report to foster understanding. Such identification does not imply recommendation or endorsement by the National Institute of Standards and Technology, nor does it imply that the materials or equipment identified are necessarily the best available for the purpose.

7 The uncertainty is based on repeated calibrations against NIST’s primary pressure standard. The stated uncertainty includes the standard deviation of fit residuals, hysteresis, reproducibility, and the uncertainty from the primary pressure standard.

$$u(\Delta P_{1n}) = \sqrt{u^2(\Delta P_{\text{cal}}) + u^2(\Delta P_{\text{zero}})} \quad (4A)$$

for $n = 2$ to 4 , where ΔP_{1n} is the measured differential pressure, and $u(\Delta P_{\text{cal}})$ is the dimensional uncertainty (in units of pressure) attributed to the calibration of the transducer.

The pressure difference between ports 1 and 2 (ΔP_{12}) has special significance and is denoted “*velocity pressure*”. Two other important differential pressure measurements include the “*yaw pressure*” and the “*pitch pressure*”. The yaw pressure is the differential pressure between ports 2 and 3 (ΔP_{23}) while the pitch pressure is the differential pressure between ports 4 and 5 (ΔP_{45}). Since NIST measured all the probe differential pressures relative to port 1, we subtract the appropriate differential pressure measurements to determine the yaw pressure and the pitch pressure. The yaw pressure is $\Delta P_{13} - \Delta P_{12}$ and the pitch pressure is $\Delta P_{15} - \Delta P_{14}$.

The uncertainty in the velocity pressure measurement (ΔP_{12}) is given by Eq. (4A). However, additional considerations are necessary to determine the uncertainty of the yaw pressure (ΔP_{23}) and the pitch pressure (ΔP_{45}) since each is determined by the difference of two separate measurements. The yaw pressure will be zero at the yaw-null condition so that the two pressure measurements ΔP_{13} and ΔP_{12} will be nearly identical. In this case, the uncertainty from calibrating both transducers to the same standard is perfectly correlated, and does not contribute to the uncertainty of ΔP_{13} and ΔP_{12} . In contrast, the uncertainty from zero drift is not correlated and must be included for both transducers. Consequently, the uncertainty for the yaw pressure at (or near) the yaw condition is

$$u(\Delta P_{23}) = \sqrt{2} u(\Delta P_{\text{zero}}) \quad (4B)$$

where the factor $\sqrt{2}$ accounts for the zero drift of both transducers. For the uncertainty in the pitch pressure, the two measurements ΔP_{15} and ΔP_{14} are not equal, and their uncertainties of their calibrations are not correlated. In this case the uncertainty is

$$u(\Delta P_{45}) = \sqrt{2u^2(\Delta P_{\text{cal}}) + 2u^2(\Delta P_{\text{zero}})} \quad (4C)$$

where $\sqrt{2}$ is a factor of both $u(\Delta P_{\text{cal}})$ and $u(\Delta P_{\text{zero}})$.

We leak checked each pressure line before calibration to prevent erroneous pressure readings resulting from leaks.

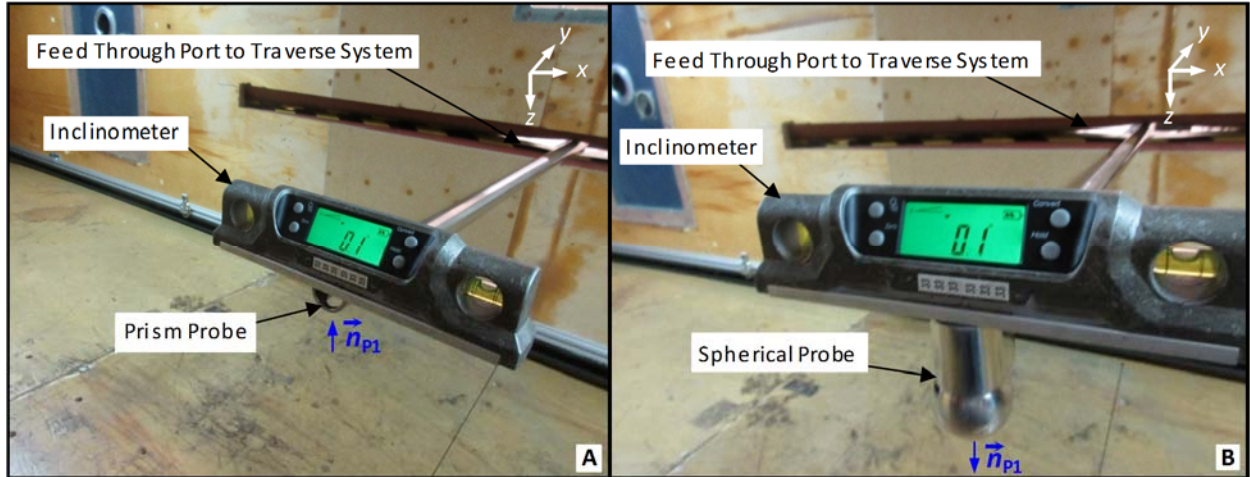


Figure 4. Yaw angle alignment: (A) Prism probe, and (B) Spherical probe in wind tunnel test section. Flow moves in the positive x-direction.

3.2 Alignment of 5-hole Probes

Figures 4A and 4B show pictures of the yaw angle alignment of both the prism probe and the spherical probe in the wind tunnel test section. The inclinometer in each figure is balanced on the flat sections of each probe head. The probe shaft is rotated until the inclinometer reads zero within $\pm 0.5^\circ$. At these reference yaw angles, the vector normal to port 1 (shown as \vec{n}_{p1} in the figures) is orthogonal to the axis of the wind tunnel (the x-axis). In Fig. 4A port 1 on the prism probe is oriented upwards in the direction of \vec{n}_{p1} so that the yaw angle is -90° . In contrast, port 1 on the spherical probe shown in Fig. 4B is oriented downward in the direction of \vec{n}_{p1} so that the yaw angle is 90° . Based on this convention the yaw angle is zero when the probe is rotated so that \vec{n}_{p1} points into the oncoming flow (*i.e.*, \vec{n}_{p1} is parallel to but opposite the x-axis).

We define the pitch angle equal to zero when the probe axis is parallel to the transverse direction depicted by the y-axis in Fig. 4A and 4B. The traverse system is used to align probe to the zero-pitch position. The standard uncertainty of rotating a probe to the zero-pitch position and to all pitch angles $\pm 45^\circ$ is $u(\alpha) = 0.25^\circ$.

The standard uncertainty of the yaw angle is $u(\theta) = 0.32^\circ$. The yaw angle uncertainty is given by

$$u(\theta) = \sqrt{u_{\text{ALIGN}}^2(\theta) + u_{\text{TRAV}}^2(\theta)} \quad (5)$$

where $u_{\text{ALIGN}}(\theta)$ is the standard uncertainty attributed to yaw angle misalignment incurred during probe installation, and $u_{\text{TRAV}}(\theta)$ is the standard uncertainty associated with the traversing system's rotary encoder. The standard uncertainty attributed to yaw angle misalignment is $u_{\text{ALIGN}}(\theta) = \pm 0.5^\circ / \sqrt{6} \cong \pm 0.2^\circ$ where $\pm 0.5^\circ$ is accuracy of the inclinometer shown in Fig. 4. Assuming a triangular distribution, the standard uncertainty is obtained by dividing $\pm 0.5^\circ$ by $\sqrt{6}$ [12].

4 CALIBRATION PROCEDURES AND RESULTS

We calibrated both the spherical and prism probes using the framework of the Method 2F procedure. Deviations from the Method 2F procedure are discussed in detail. The spherical probe was calibrated on 3 different occasions: 7/12/2016, 7/15/2016, and 11/1/2016 while the prism probe was calibrated on 2 occasions: 7/18/2016 and 7/22/2016. The calibration conditions (*i.e.*, the range of air speeds, pitch angles, and yaw angles) are listed in Table 1 for the spherical probe and in Table 2 for the prism probe.

Table 1. Calibration conditions for the 5-hole spherical probe.

No.	Date	Range of LDA Velocities (V_{LDA})	Range of Pitch Angles (α)	Range of Yaw Angles (θ)
1	7/12/2016	5 m/s to 30 m/s (5 m/s steps)	-45° to 45° (3° steps)	-9° to 9° (3° steps, $N = 7$)
2	7/15/2016	7.5 m/s to 27.5 m/s (5 m/s steps)	-43.5° to 43.5° (3° steps)	-7.5° to 7.5° (3° steps, $N = 6$)
3	11/1/2016	5 m/s to 30 m/s (5 m/s steps)	-45° to 45° (5° steps)	-10° to 10° (2° steps, $N = 11$)

Table 2. Calibration conditions for the 5-hole prism probe.

No.	Date	Range of LDA Velocities (V_{LDA})	Range of Pitch Angles (α)	Range of Yaw Angles (θ)
1	7/18/2016	5 m/s to 30 m/s (5 m/s steps)	-45° to 45° (3° steps)	-9° to 9° (3° steps, $N = 7$)
2	7/22/2016	7.5 m/s to 27.5 m/s (5 m/s steps)	-43.5° to 43.5° (3° steps)	-7.5° to 7.5° (3° steps, $N = 6$)

After installing the probe into the traversing system and leak checking each pressure line, the air speed in the wind tunnel is set to the lowest-velocity set point and allowed to stabilize. While the air speed is stabilizing, the traverse system moves the probe to the initial pitch and yaw angles. After the pressure readings and the air speed are stable, we record the differential pressure readings from the probe (*i.e.*, ΔP_{12} , ΔP_{13} , ΔP_{14} , and ΔP_{15}), the LDA velocity (V_{LDA}), the static pressure, static temperature, and relative humidity. Subsequently, the probe is rotated to the next yaw angle and another set of data is recorded. We repeat this procedure until data is acquired at all the prescribed yaw angles. After traversing the range of pitch angles, we repeat the entire procedure from the beginning at the next air speed set point.

4.1 Null Parameters and Calibration Factors

At each air speed and pitch angle, we measured the yaw-null angle (θ_{NULL}) by determining the yaw angle for which the yaw pressure is zero (*i.e.*, $\Delta P_{23} = 0$). At the yaw-null angle we also measured the null pitch pressure ($\Delta P_{45, NULL}$) and the null velocity pressure ($\Delta P_{12, NULL}$). These null-parameters are used in conjunction with the measured air speed (V_{LDA}) and air density (ρ) to

determine the *pitch angle calibration factor* (F_1) and the *velocity calibration factor* (F_2). The formulas used to compute the pitch angle calibration factor and the velocity calibration factor are:

$$F_1 = \frac{(P_4 - P_5)_{\text{NULL}}}{(P_1 - P_2)_{\text{NULL}}} = \frac{\Delta P_{45,\text{NULL}}}{\Delta P_{12,\text{NULL}}}, \quad (6A)$$

and

$$F_2 = C_{\text{LDA}} \sqrt{\frac{\Delta P_{\text{dyn}}}{(P_1 - P_2)_{\text{NULL}}}} = C_{\text{LDA}} \sqrt{\frac{\Delta P_{\text{dyn}}}{\Delta P_{12,\text{NULL}}}} = \sqrt{\frac{\rho V_{\text{LDA}}^2}{2 \Delta P_{12,\text{NULL}}}}, \quad (6B)$$

respectively. In Eq. (6B) the dynamic pressure is calculated from Eq. (1) so that the coefficient C_{LDA} is identically equal to 1.

4.2 Curve Fit Method (CFM) to Determine the Null Parameters

When using the CFM one does not attempt to rotate the probe to the exact position where the yaw pressure is zero; instead, one measures each of the five physical variables shown in Table 3 over a narrow range of yaw pressures surrounding $\Delta P_{23} = 0$. Then, the measured values are fitted to a polynomial function of the yaw pressure, which is evaluated at $\Delta P_{23} = 0$ to give the respective null parameters (e.g., θ_{NULL} , $\Delta P_{45,\text{NULL}}$, and $\Delta P_{12,\text{NULL}}$). We use the notation Γ_q to represent any of the five quantities listed in Table 3 where the subscript “q” identifies each quantity. The measured values are compactly expressed as ordered pairs $(\Delta P_{23,n}, \Gamma_{q,n})$, where the subscript n denotes the n^{th} measurement of the N total measurements made at the points listed in Table 1 for the spherical probe and in Table 2 for the prism probe.

Table 3. Definition of the Generic Probe Parameters ($\Gamma_{q,n}$)

θ	Physical Variable	Generic Probe Parameters
1	yaw angle, (θ)	$\Gamma_1 = \theta$
2	pitch pressure, (ΔP_{45})	$\Gamma_2 = \Delta P_{45}$
3	velocity pressure, (ΔP_{12})	$\Gamma_3 = \Delta P_{12}$
4	pitch pressure ratio, (PR_1) ^a	$\Gamma_4 = PR_1 = \Delta P_{45}/\Delta P_{12}$
5	velocity pressure ratio, (PR_2) ^b	$\Gamma_5 = PR_2 = \sqrt{\Delta P_{\text{LDA}}/\Delta P_{12}}$

^aBy definition, the pitch pressure ratio equals the pitch calibration factor, $PR_1(0) = F_1$ at zero yaw pressure.

^bBy definition, the velocity pressure ratio equals the velocity calibration factor $PR_2(0) = F_2$ at zero yaw pressure.

The N data points $(\Delta P_{23,n}, \Gamma_{q,n})$ are fit to a 4th degree polynomial given by⁸

$$\Gamma_{q,\text{FIT}} = a_0 + a_1 \Delta P_{23} + a_2 \Delta P_{23}^2 + a_3 \Delta P_{23}^3 + a_4 \Delta P_{23}^4 \quad (7)$$

where a_0 , a_1 , a_2 , a_3 , and a_4 , are the fit coefficients, and $\Gamma_{q,\text{FIT}}$ is the fitted function. The fit is used as a continuous extension of the discrete data set; therefore, the null parameters are determined by evaluating the curve fit at zero-yaw pressure,

8 At some large (positive and negative) pitch angles we used a 3rd degree polynomial.

$$\Gamma_{q,\text{FIT}}(0) = \Gamma_{q,\text{NULL}} = a_{q,0} \quad (8)$$

where $a_{q,0}$ is the zeroth-degree fit coefficient (*i.e.*, y -intercept of the polynomial fit) and the subscript “ q ” specifies the quantity that is being evaluated, as shown in Table 3. For example, for $q = 1, 2,$ and 3 the corresponding null parameters are: $a_{1,0} = \theta_{\text{NULL}}$; $a_{2,0} = \Delta P_{45,\text{NULL}}$; and $a_{3,0} = \Delta P_{12,\text{NULL}}$, while for $q = 4$ and 5 the calibration coefficients are: $a_{4,0} = F_1$ and $a_{5,0} = F_2$.

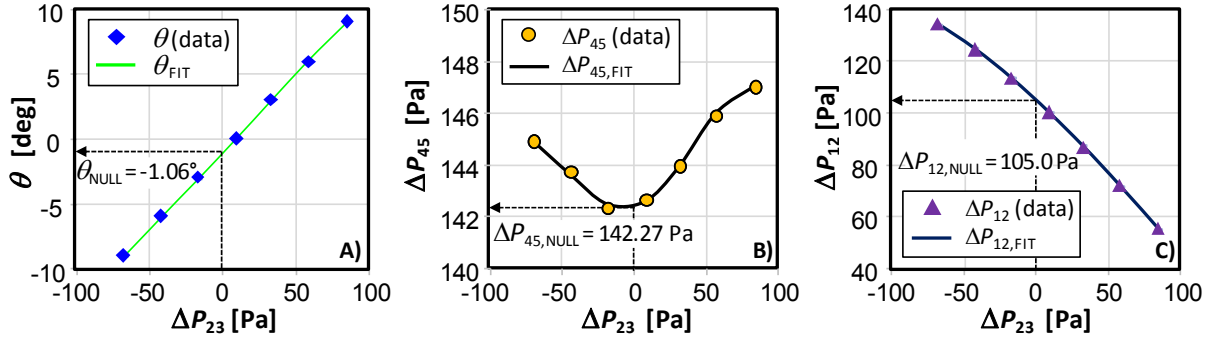


Figure 5. Plots of the A) the yaw angle (\blacklozenge), B) the pitch pressure (\bullet), and C) the velocity pressure (\blacktriangle) versus the yaw angle for the spherical probe at an air speed of 15 m/s and a pitch angle of 21° . A 4th degree curve fit evaluated at $\Delta P_{23} = 0$ gives a yaw-null angle of $\theta_{\text{NULL}} = -1.06^\circ$, a pitch pressure at the yaw-null angle of $\Delta P_{45,\text{NULL}} = 142.27$ Pa, and a velocity pressure at the yaw-null angle of $\Delta P_{12,\text{NULL}} = 105.0$ Pa.

Figure (5) shows an example of how the null parameters are computed for the spherical probe at $V_{\text{LDA}} = 15$ m/s and $\alpha = 21^\circ$. The measured yaw angles (\blacklozenge), pitch pressures (\bullet), and velocity pressures (\blacktriangle) are plotted along with their corresponding polynomial curve fits indicated by the solid lines (—). The dashed line (---) in each plot originates vertically from x -axis, intercepts the polynomial fit at $\Delta P_{23} = 0$, and extends horizontally to the y -axis where it indicates the value of respective null parameter. For the air speed and pitch angle in this example, Fig. (5A) shows the yaw-null angle equals $\theta_{\text{NULL}} = -1.06^\circ$. Fig. (5B) shows the pitch pressure at the null angle is $\Delta P_{45,\text{NULL}} = 142.27$ Pa, and Fig. (5C) depicts that the velocity pressure at the null angle is $\Delta P_{12,\text{NULL}} = 105.0$ Pa. The measured null parameters along with the air speed and air density are used to calculate F_1 and F_2 and *via* Eqs. (6A) and (6B). For this example, these values are $F_1 = 1.358$ and $F_2 = 1.121$, respectively.

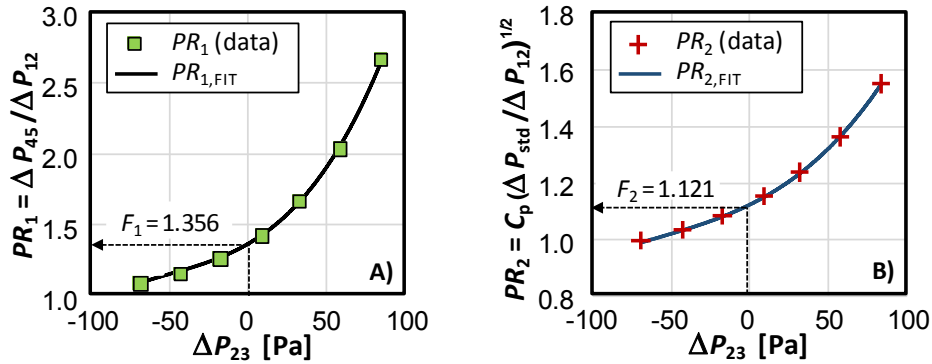


Figure 6. Plots of the A) the pitch pressure ratio (\blacksquare) and B) the velocity pressure ratio ($+$) versus the yaw pressure for the spherical probe at an air speed of 15 m/s and a pitch angle of 21° . A 4th degree curve fit evaluated at $\Delta P_{23} = 0$ gives the pitch calibration factor of $F_1 = 1.356$ and a velocity calibration factor of $F_2 = 1.121$.

As indicated in the last two rows of Table 3, the calibration factors F_1 and F_2 can be directly calculated using the CFM to evaluate pitch pressure ratio (PR_1) and the velocity pressure ratio (PR_2) at $\Delta P_{23} = 0$. Figure (6) illustrates how this is done. The pitch calibration factor (F_1) is determined by curve fitting PR_1 (■) versus the yaw pressure in Fig. (6A) and evaluating the fit at $\Delta P_{23} = 0$. Similarly, the velocity calibration factor (F_2) is the y -intercept of the curve fit of PR_2 (+) versus the yaw pressure shown in Fig. (6B). The difference in the values of F_1 and F_2 calculated by evaluating PR_1 and PR_2 at $\Delta P_{23} = 0$ shown in Fig. (6) are metrologically equivalent (*i.e.*, within the uncertainty) with F_1 and F_2 computed using the values of $\Delta P_{45, \text{NULL}}$ in Fig. (5B) and $P_{12, \text{NULL}}$ in Fig. (5C) along with Eqs. (6A) and (6B). Although both methods give equivalent results, in this work we opt to calculate the null parameters using Eqs. (6A) and (6B) as this choice facilitates a slightly easier uncertainty analysis.

4.3 Calibration Results for a Spherical Probe

Figure 7 shows the calibration data of the spherical probe performed on 7/12/2016. Figures 7A and 7B show F_1 and F_2 , respectively, plotted as a function of the pitch angle α . Each symbol in the figure corresponds to one of the 6 air speed set points (V_n 's) shown in the legend. Each of these velocities is measured by the LDA system. In Fig. 7A, the pitch angle calibration factor F_1 is approximately a linear function of α at pitch angles above -30° . In Fig. 7B, the values of F_2 are approximately a parabolic function of α . Although Figs. 7A and 7B display the trends of F_1 and F_2 , they do not reveal the details of the velocity-dependences of F_1 and F_2 .

The velocity-dependences of F_1 and F_2 are shown more clearly in Figs. 7C and 7D, respectively. Figure 7C plots the difference $F_1(V_n) - F_1(20 \text{ m/s})$, where $F_1(V_n)$ is evaluated at air speeds V_n indicated by the legend above Fig. 7 and $F_1(20 \text{ m/s})$ is the reference value at 20 m/s. Similarly, Fig. 7D is a plot of the percent difference $100 \times [F_2(V_n)/F_2(20 \text{ m/s}) - 1]$ between $F_2(V_n)$ and reference value $F_2(20 \text{ m/s})$. Plotting the calibration factors relative to the reference values clearly shows that F_1 and F_2 are velocity-dependent. The velocity-dependence is largest at pitch angles $\alpha < -30^\circ$ and $\alpha > 40^\circ$. For large negative pitch angles, the values of $F_2(V_n)$ deviate by as much as 10 % from the reference value. However, for pitch angles $\alpha > -25^\circ$ the velocity-dependence of $F_2(V_n)$ is less than 1 % of F_2 , except for a fraction of the data at the lowest air speed $V_1 = 5 \text{ m/s}$. These results show that one could calibrate a spherical probe at a single reference velocity of 20 m/s and at a single pitch angle $\alpha = 0^\circ$, and then apply the calibration to a wider range of

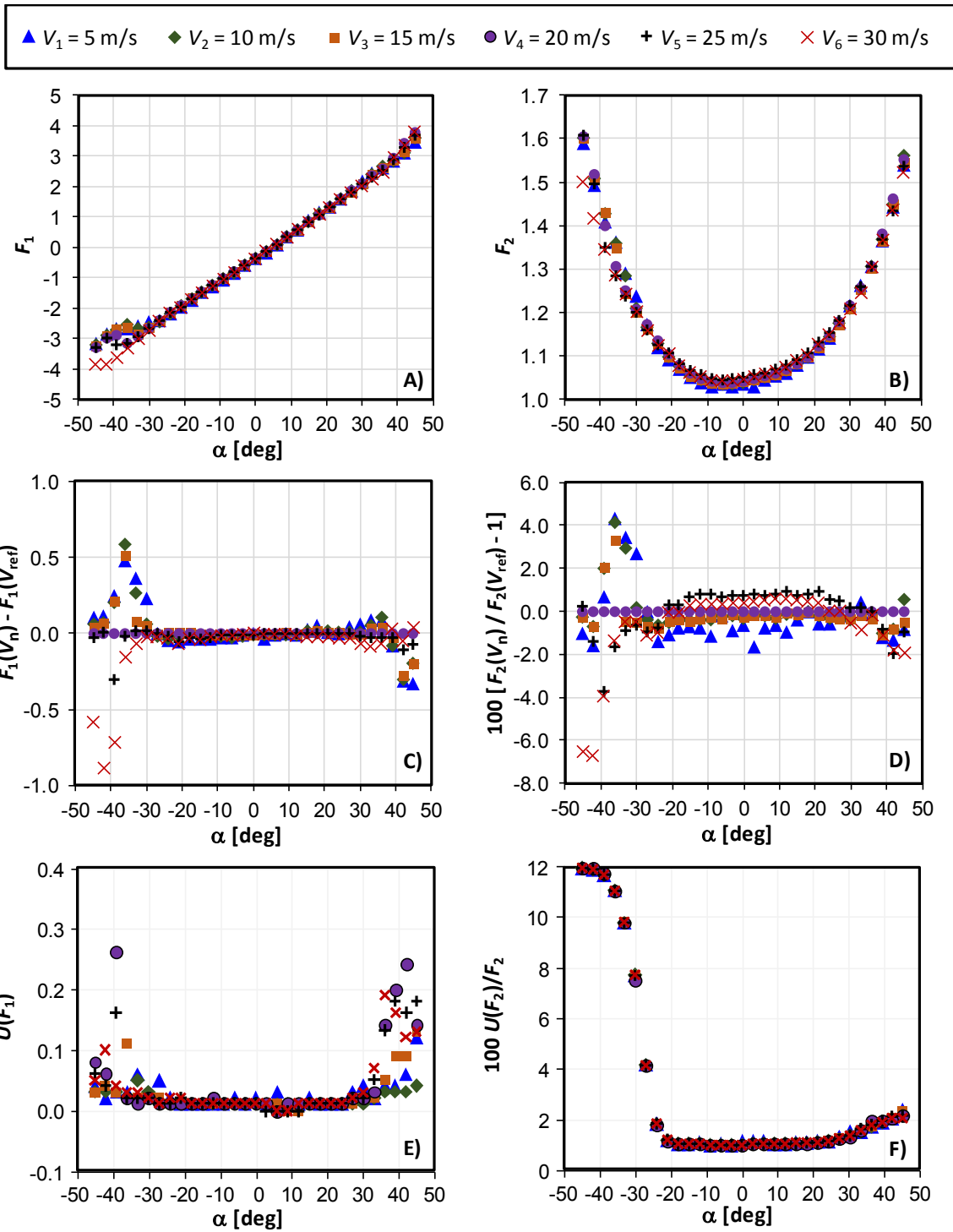


Figure 7. Calibration results of Spherical Probe for 6 air speeds ranging from 5 m/s to 30 m/s as functions of pitch angle α . A) pitch calibration factor, F_1 ; B) velocity calibration factor, F_2 ; C) difference between F_1 at specified air speeds and a reference value at an air speed of 20 m/s; D) percentage difference between F_2 at specified air speeds and a reference value at an air speed at 20 m/s; E) expanded uncertainty of F_1 at 95 % confidence level; F) expanded percentage uncertainty of F_2 at 95 % confidence level.

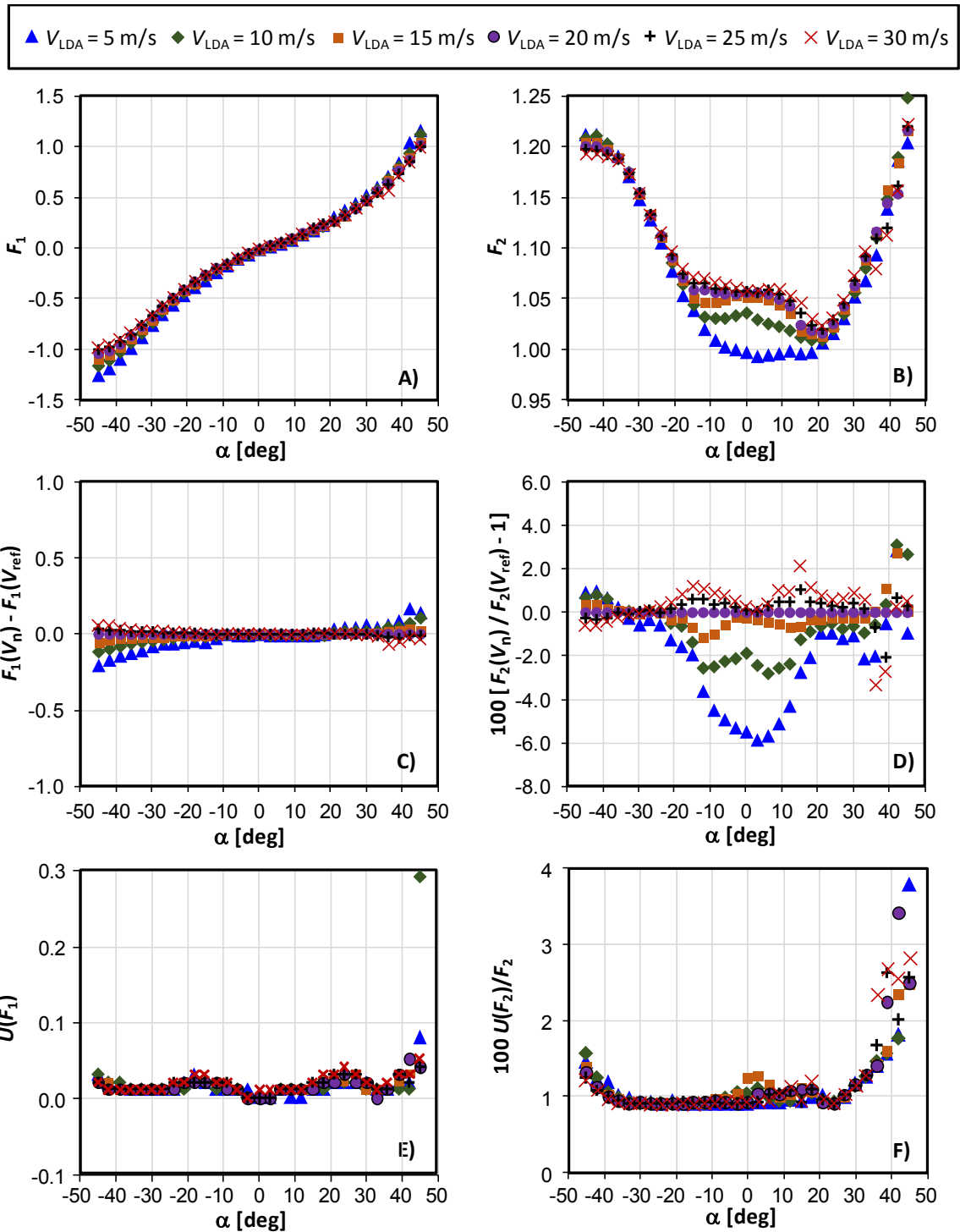


Figure 8. Calibration results of Prism Probe for 6 air speeds ranging from 5 m/s to 30 m/s as functions of pitch angle α . A) pitch calibration factor, F_1 ; B) velocity calibration factor, F_2 ; C) difference between F_1 at specified air speeds and F_1 at the reference air speed of 20 m/s; D) percentage difference between F_2 at specified air speeds and F_2 at the reference air speed at 20 m/s; E) expanded uncertainty of F_1 at 95 % confidence level; F) expanded percentage uncertainty of F_2 at 95 % confidence level.

airspeeds ($10 \text{ m/s} \leq V_{\text{LDA}} \leq 30 \text{ m/s}$) and pitch angles ($-25^\circ \leq \alpha \leq 35^\circ$). The values of F_2 determined from such a single-point calibration would be within $\pm 1\%$ of the values of F_2 , as determined via the complete calibration.⁹

Figure 7E shows the expanded uncertainty $U(F_1)$ of the calibration factor F_1 and Fig 7F shows the percent expanded uncertainty $100 \times U(F_2)/F_2$. The expanded uncertainty is defined as the confidence interval that includes 95 % of the F_1 and F_2 data. The uncertainties $U(F_1)$ and $U(F_2)$ have two sources: 1) the uncertainty attributed to the reproducibility of repeated calibrations, and 2) the *data reduction uncertainty*, which combines uncertainty contributions from all the auxiliary variables used to calculate F_1 and F_2 . Section 4.5 documents the reproducibility uncertainties, and Section 5 documents the data reduction uncertainties.

The uncertainties of both calibration factors increased at the extreme positive and negative values of pitch. The sharp increase of $U(F_2)$ at pitch angles below $\alpha < -30^\circ$ is primarily attributed to the random uncertainty, which is calculated by the standard deviation of repeated measurements. We speculate that this large random uncertainty results from complex flow patterns over the temperature probe and its protective cylindrical tip (See Fig. 1B.). At large negative pitch angles, the vortices shed from these obstacles are likely to interfere with the differential pressure measurements between the ports, thereby resulting in a large random component of uncertainty.

4.4 Calibration Results for a Prism Probe

Figure 8 shows the calibration data of the prism probe performed on 7/18/2016. The calibration factors F_1 and F_2 are plotted as a function of the pitch angle α in Figs. 8A and 8B, respectively. Each plotted symbol corresponds to one of the 6 velocity set points V_n shown in the legend. In contrast to the spherical probe, the prism probe's F_2 calibration factor has a strong Re -dependence at pitch angles in the range $-20^\circ \leq \alpha \leq 20^\circ$. As shown in Fig. 8D, the values of $F_2(V_n)$ span a range of 6 %. [Fig. 8D plots the percentage difference between the velocity calibration factor at different air speeds V_n and a reference value at $V_{\text{ref}} = 20 \text{ m/s}$, $100 \times [F_2(V_n)/F_2(20 \text{ m/s}) - 1]$. Analogously, Fig. 8C is a plot of the differences $F_1(V_n) - F_1(20 \text{ m/s})$. As shown in Fig. 8C, F_1 is independent of velocity for pitch angles in the range $-10^\circ \leq \alpha \leq 20^\circ$; however, outside this range F_1 becomes increasingly velocity dependent. Because of the prism probe's velocity dependence, it should be calibrated over the range of air speeds it will be used in stack measurement applications to achieve better accuracy.

The expanded uncertainties of the calibration coefficients $U(F_1)$ and $100 \times U(F_2)/F_2$ and are plotted in Figs. 8E and 8F. The uncertainty of F_1 is nearly independent of pitch angles in the range $-40^\circ \leq \alpha \leq 40^\circ$; it increases when $\alpha > 40^\circ$. As shown in Fig. 8F, the expanded uncertainty $100 \times U(F_2)/F_2$ increases sharply at large positive ($\alpha > 40^\circ$) and negative ($\alpha < -40^\circ$) pitch angles. For pitch angles $-30^\circ \leq \alpha \leq 0^\circ$ the expanded uncertainty is approximately a constant value of 0.9 %. In the range $0^\circ \leq \alpha \leq 20^\circ$, the expanded uncertainty increases only slightly, reaching a maximum value of 1.25 %.

4.5 Probe Reproducibility and Rational Polynomial Curve Fits of the Calibration Data

During a EPA stack emissions testing commonly called a relative accuracy test audit (RATA), the axial velocity along the stack axis (V_z) is determined by the equation:

⁹ While this observation applies for the laminar flow conditions used in this calibration, more research is needed to confirm it applies in turbulent flow.

$$V_x = F_2 \sqrt{\frac{2\Delta P_{12, \text{NULL}}}{\rho}} \cos(\theta_{\text{NULL}}) \cos(\alpha) \quad (9)$$

where the velocity pressure $\Delta P_{12, \text{NULL}}$ and the yaw-null angle θ_{NULL} are measured using the Method 2F nulling procedure. The pitch pressure is also measured at the null condition $\Delta P_{45, \text{NULL}}$ and used along with $\Delta P_{12, \text{NULL}}$ to calculate the pitch calibration factor F_1 via Eq. (6A). In contrast, the pitch angle α and velocity calibration factor F_2 are not measured during a RATA test, but instead are based on curve fits of the probe calibration data. For a specified probe shape, the calibration factors F_1 and F_2 are characterized by the pitch angle, Reynolds number (or airspeed), and turbulence intensity.¹⁰ For some probe shapes the Re -dependence is significant (e.g., see prism probe results for F_2 in Fig. 8D) while for other probes the Re -dependence is small (e.g., see spherical probe results for F_2 in Fig. 7D).

Here, we provide high-accuracy curve fits to the pitch angle and the velocity calibration factor. These fits account for Reynolds number effects and are valid for airspeeds spanning the range $5 \text{ m/s} \leq V \leq 30 \text{ m/s}$ and for pitch angles $-45^\circ \leq \alpha \leq 45^\circ$. We use a rational polynomial fit expressed by

$$\Psi_{\text{FIT}, p} = \frac{\sum_{m=0}^N \sum_{n=0}^{N-m} a_{mn, p} x_p^m y_p^n}{\sum_{m=0}^N \sum_{n=0}^{N-m} b_{mn, p} x_p^m y_p^n} \quad (10)$$

where the numerator and denominator are each $N = 5$ degree polynomials of the two variables x_p and y_p . The fit was developed using the commercial available software package Origin.⁶ The index “p” ranges from 1 to 3; it identifies the fitting functions $\Psi_{\text{FIT}, p}$, and their dependent variables x_p and y_p , as shown in Table 4. Using this compact notation, the symbol $\Psi_{\text{FIT}, p}$ represents three fitted functions; 1) $\Psi_{\text{FIT}, 1} = \alpha_{\text{FIT}}$ is the pitch angle fitted to the dependent variables $\Delta P_{45, \text{NULL}}$ and F_1 ; 2) $\Psi_{\text{FIT}, 2} = F_{2, \text{FIT}}$ is the velocity calibration factor fitted to the dependent variables α_{FIT} and $(\Delta P_{12, \text{NULL}})^{1/2}$, and 3) $\Psi_{\text{FIT}, 3} = \Delta P_{\text{std}, \text{FIT}}$ is the standard pressure fitted to the dependent variables $(\Delta P_{12, \text{NULL}})^{1/2}$ and F_1 . The third function $\Psi_{\text{FIT}, 3}$ can be used instead of $\Psi_{\text{FIT}, 2}$ to determine the flow velocity. In this case the grouped-terms $F_2^2 \Delta P_{12, \text{NULL}}$ in Eq. (9) are replaced by ΔP_{std} so that the axial velocity is expressed in terms of the standard pressure, $V_x = \sqrt{2\Delta P_{\text{std}} / \rho} \cos(\theta_{\text{NULL}}) \cos(\alpha)$.

Table 4. Rational polynomial fits for α , F_2 , and ΔP_{std} .

p	x_p	y_p	$\Psi_{\text{FIT}, p}$
1	$\Delta P_{45, \text{NULL}}$, [Pa]	F_1 , []	α_{FIT} , [deg]
2	α_{FIT} , [deg]	$\sqrt{\Delta P_{12, \text{NULL}}}$, [Pa ^{1/2}]	$F_{2, \text{FIT}}$, []
3	$\sqrt{\Delta P_{12, \text{NULL}}}$, [Pa ^{1/2}]	F_1 , []	$\Delta P_{\text{std}, \text{FIT}}$, [Pa]

¹⁰ The effect of turbulence intensity on the calibration factors is a topic of current research and is beyond the scope of this document. Preliminary studies show that a 10 % turbulence intensity has a 2 % - 3 % effect on the velocity calibration factor, F_2 .

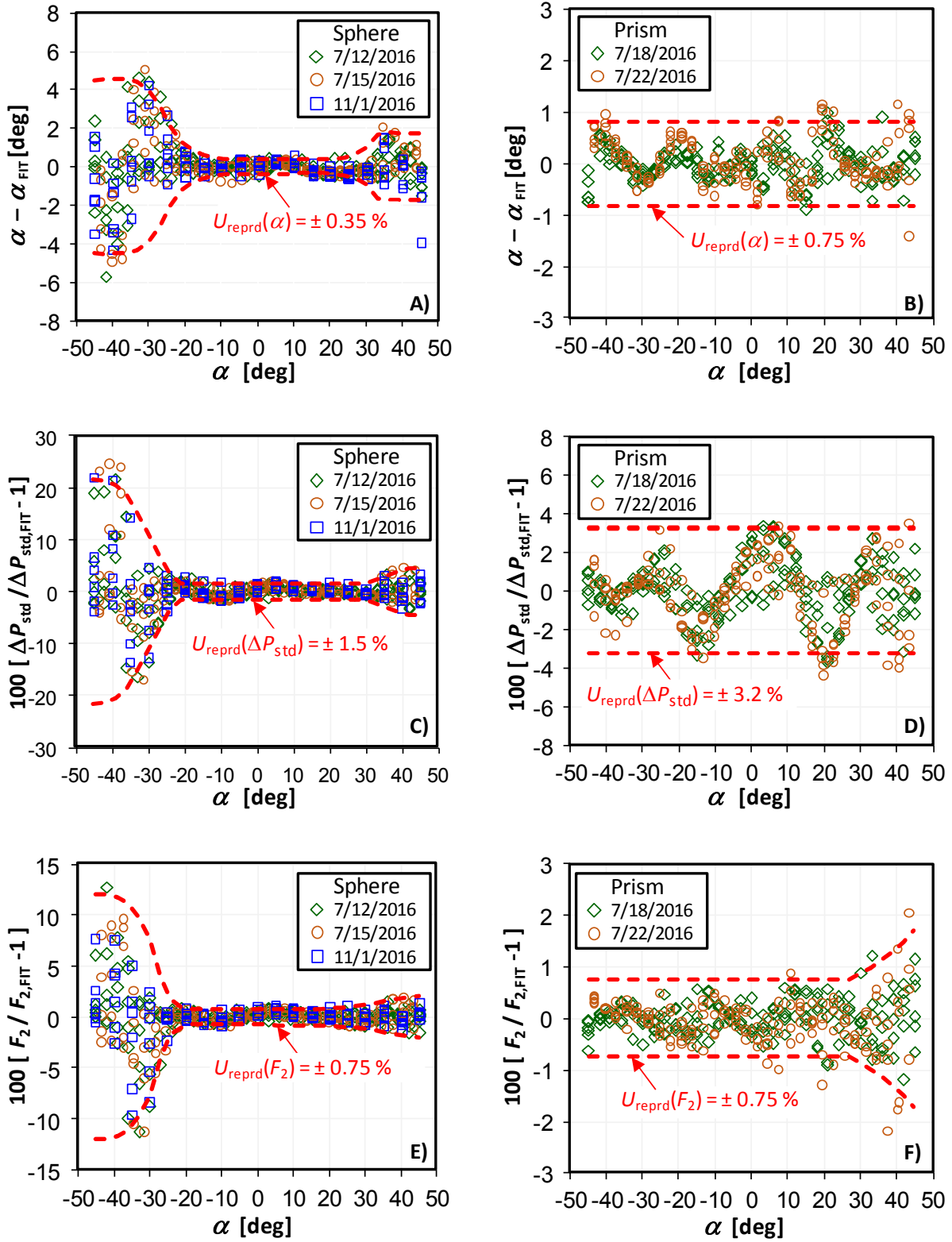


Figure 9. Residuals from Eqs. (10), rational polynomials fitted to 3 repeated calibrations of the spherical probe (left) and the 2 repeated calibrations of the prism probe (right). The residuals are plotted versus the pitch angle α for 6 air speeds ranging from 5 m/s to 30 m/s. The dashed lines (---) enclose 95 % of the data.

The residuals of the three fitted functions $\Psi_{\text{FIT},p}$ from the corresponding measured values are plotted as a function of pitch angle in Fig. 9. Figures 9A, 9C, and 9E are plots of the residuals from three repeated calibrations of the spherical probe; Figs. 9B, 9D, and 9F are plots of the residuals from two calibrations of the prism probe. For comparisons, the residuals from the two probes are plotted next to each other. (Note: the vertical scales for the spherical probe span wider ranges than the corresponding scales for the prism probe.) Figures 9A and 9B plot the pitch angle residual $\alpha - \alpha_{\text{FIT}}$. Figures 9C and 9D plot as a percent, the residual of the fitted standard pressure from the measured pressure $100 \times [\Delta P_{\text{std}} / \Delta P_{\text{std,FIT}} - 1]$. Figures 9E and 9F plot as a percent, the residual of the fitted velocity factor from the measured velocity factor $100 \times [\Delta F_2 / \Delta F_{2,\text{FIT}} - 1]$.

The dashed lines (---) are confidence intervals containing 95 % of the data. If data in the confidence intervals were randomly distributed, these confidence intervals would be a measure of the reproducibility U_{reprd} of repeated calibrations. In Fig. 9D, the averaged data at some of the pitch angles is not zero, indicating that the deviations are not completely random. A better curve fit could reduce these deviations; thereby, reducing U_{reprd} . Thus, the structure in the residual plots cause the values of U_{reprd} to be biased high. Nevertheless, we use this measure to estimate the reproducibility of the calibration factors, and the uncertainties attributed to reproducibility of F_1 and F_2 are included in the respective uncertainty budgets for the spherical probe in Section 4.3 and the prism probe in Section 4.4.

Care must be taken when comparing residual plots of the spherical probe to those of the prism probe because the scales on the y-axes are not the same. However, it is clear all the residual plots of the spherical probe sharply increase at large negative pitch values. In Section 4.3 we hypothesized that at large negative pitch angles the pressure ports are engulfed by a turbulent wake. The wake is caused by vortices shed from the temperature sensor and the cylindrical tip located just upstream of the probe ports (see probe geometry in Fig. 1B) at large negative pitch angles. The inherent fluctuations in the wake result in the larger reproducibility for $\alpha < -20^\circ$. In field RATA tests, pitch angles are usually greater than -20° ; therefore, this reproducibility will not limit the accuracy of RATA tests using spherical probes.

For pitch angles $-20^\circ \leq \alpha \leq 30^\circ$ the values of U_{reprd} for the spherical probe (See Figs. 9A, 9C, and 9E.) are uniform and are less than or equal to U_{reprd} of the prism probe. This range of pitch angles includes typical α values encountered in typical RATA tests; therefore, we expect slightly better reproducibility from a spherical probe than from a prism probe.

At large positive pitch angles ($\alpha > 30^\circ$), the reproducibility of the spherical probe is not quite as good, as evidenced by the slight increase in U_{reprd} in probe in Figs. 9A, 9C, and 9E. Figure 9F shows that the reproducibility of the velocity calibration factor for the prism probe also increases at large positive pitch angles. The reproducibility at large positive pitch angles, like that of large negative pitch angles, does not play a role in field RATA tests where pitch angles are typically $-20^\circ \leq \alpha \leq 20^\circ$.

5 UNCERTAINTY ANALYSIS OF CALIBRATION RESULTS

In this section we calculate the expanded uncertainty of the yaw-null angle θ_{NULL} , the pitch pressure at the null condition $\Delta P_{45,\text{NULL}}$, the velocity pressure at the null condition $\Delta P_{12,\text{NULL}}$, and the calibration factors F_1 and F_2 . These uncertainties are calculated for airspeeds $5 \text{ m/s} \leq V_{\text{LDA}} \leq 30 \text{ m/s}$ and pitch angles from $-45 \leq \alpha \leq 45$. The uncertainties of the pitch (F_1) and velocity (F_2) calibration factors are plotted in Figs. 7E and 7F for the spherical probe, and in Figs. 8E and 8F for the prism probe. In most stack applications, the maximum range of the pitch

angle is $-20 \leq \alpha \leq 20$. For this narrower range of pitch angles the expanded uncertainty of F_2 is nearly constant for both probes; for the spherical probe, $U_r(F_2)$ ranges from 0.9 % to 1.1 % while for the prism probe, $U_r(F_2)$ ranges from 0.9 % to 1.25 %. For both probes the largest uncertainty sources for F_2 are the reproducibility of repeated calibrations and the LDA standard, which together, contributed 60 % to 80 %.

The methodical uncertainty calculations provided herein are intended both to document these results and to provide guidance to those in stack testing community or other metrologist not as familiar with uncertainty analysis. Those not interested in these details can skip this section without loss of continuity.

5.1 Data Reduction Equation and Method of Propagation of Uncertainty

The uncertainty analysis is based on the method of propagation of uncertainty [13,14]. In this method, a mathematical expression called the *data reduction equation* relates the functional dependence of one or more measured input quantities to an output quantity. Equation (11) is a generic data reduction equation

$$y = y(x_1, x_2, \dots, x_M), \quad (11)$$

that relates M input quantities given by the x_m 's to a single output y . Several data reduction equations have been used throughout this work; for example, the air density ρ in Eq. (2) is not measured directly, but is calculated from its data reduction equation, which has as its inputs the measured pressure P , temperature T , and relative humidity RH . Likewise, the pitch calibration factor F_1 is calculated from its data reduction equation given in Eq. (6A), which has as its inputs $\Delta P_{45, \text{NULL}}$ and $\Delta P_{12, \text{NULL}}$.

Propagated Uncertainties

The same data reduction equation that computes the value of an output quantity as a function of known input quantities is also used to relate the uncertainty of the M input quantities, $u(x_m)$'s, to the uncertainty of the output quantity, $u_{c,p}(y)$, called the *standard combined, propagated uncertainty*. That is, the uncertainty of an output quantity is determined by propagating the known uncertainties of the input quantities through the corresponding data reduction equation. For the generic data reduction equation given by Eq. (11) the standard combined, propagated uncertainty is

$$u_{c,p}(y) = \sqrt{\sum_{m=1}^M \left(\frac{\partial y}{\partial x_m} \right)^2 u^2(x_m) + \sum_{m=1}^M \sum_{n=1}^M (1 - \delta_{mn}) \left(\frac{\partial y}{\partial x_m} \right) \left(\frac{\partial y}{\partial x_n} \right) r(x_m, x_n) u(x_m) u(x_n)} \quad (12A)$$

where $u_{c,p}(y)$ is the uncertainty at the 68 % confidence level, the $u(x_m)$'s are the standard uncertainties of the input quantities at the 68 % confidence level; the $\partial y / \partial x_m$'s are the dimensional sensitivity coefficients equal to the partial derivatives of the output variable (y) with respect to each input variable (x_m); δ_{mn} is the *Kronecker delta function*, which equals 1 if $m = n$ and 0 if $m \neq n$; and $r(x_m, x_n)$ is the normalized correlation function, which indicates the degree of correlation between x_n and x_m .

The value of the normalized correlation coefficient in Eq. (12A) has the range $-1 \leq r(x_m, x_n) \leq 1$. In many cases, its value is difficult to determine, and approximations are necessary. In the special case where all the uncertainty sources are uncorrelated $r(x_m, x_n) = 0$, and the standard combined, propagated uncertainty simplifies to

$$u_{c,p}(y) = \sqrt{\sum_{m=1}^M \left(\frac{\partial y}{\partial x_m} \right)^2 u^2(x_m)}, \quad (12B)$$

which is the root-sum-square (RSS) of the standard uncertainty of each input amplified by its sensitivity coefficient. Alternatively, if the uncertainty sources are perfectly correlated then $r(x_m, x_n) = 1$, and Eq. (12A) simplifies to

$$u_p(y) = \left| \sum_{n=1}^N \left(\frac{\partial y}{\partial x_n} \right) u(x_n) \right| \quad (12C)$$

where the propagated uncertainty equals the absolute value of the summed products of $u(x_n)$ and $\partial y / \partial x_n$.

Throughout this document most of the propagated uncertainty sources are uncorrelated, and the RSS formulation in Eq.(12B) is used. However, in Section 5.2 the uncertainty of the null parameters has partially correlated uncertainty sources and $r(x_m, x_n)$ cannot be taken to be 0 or 1, but has an intermediate value between these two limits. As such, in this section we use an approximate method similar to Coleman [14] to estimate the degree of correlation. The details are explained in Section 5.2.

Non-Propagated Uncertainties

The uncertainty in the measurand y does not derive exclusively from propagation of measurement errors in the input quantities. Herein, we use the notation $u_{c,np}(y)$ to denote the *standard combined, non-propagated uncertainties*. In this document, non-propagated uncertainties include 1) the measurement reproducibility of F_1 and F_2 , and 2) the null-parameter curve fit uncertainty.

Combined and Expanded Uncertainties

The *standard combined uncertainty* is the RSS of the standard combined, propagated uncertainty, $u_{c,p}(y)$, and the standard combined, non-propagated uncertainty, $u_{c,np}(y)$, as given by

$$u_c(y) = \sqrt{u_{c,p}^2(y) + u_{c,np}^2(y)}, \quad (13A)$$

and the expanded uncertainty is

$$U(y) = k u_c(y) = k \sqrt{u_{c,p}^2(y) + u_{c,np}^2(y)} \quad (13B)$$

where $u_c(y)$ is the standard combined uncertainty, and k is the coverage factor, which when taken equal to $k = 2$, converts the combined standard uncertainty at the 68 % confidence level to the expanded uncertainty $U(y)$ at the 95 % confidence level, ($U = k u_c$).

5.2 Uncertainty of the Null Parameters $u(\Delta P_{23, \text{NULL}})$, $u(\Delta P_{45, \text{NULL}})$, and $u(\Delta P_{12, \text{NULL}})$

Using the CFM, the null parameters are calculated numerically via a linear regression algorithm. As shown in Eq. (8) these parameters are equal to the regression coefficient $a_{q,0}$. As such, the functional dependence of $a_{q,0}$ on its input parameters is not explicitly known. In contrast, we point out that the functional dependence of the F_1 and F_2 calibration coefficients are explicitly defined

by Eqs. (6A) and (6B), respectively. Since $a_{q,0}$ cannot be characterized by such simple algebraic expressions, we represent the output of the linear regression algorithm by the following generic expression

$$a_{q,0} = a_{q,0}(\Delta P_{23_1}, \dots, \Delta P_{23_n}, \dots, \Delta P_{23_N}, \Gamma_{q,1}, \dots, \Gamma_{q,n}, \dots, \Gamma_{q,N}), \quad (14)$$

where N is the number of data points used in the curve fit as specified in Tables 1 and 2; $\Delta P_{23,n}$ is the n^{th} measurement of the yaw pressure; and $\Gamma_{q,n}$ is the n^{th} measurement of the generic probe variable defined in Table 3 of Section 4.2. The dependent variables on the right-hand side of Eq. (14) list the N data points, $(\Delta P_{23,n}, \Gamma_{q,n})$, used by the regression model to calculate $a_{q,0}$. Because $a_{q,0}$ is calculated numerically, the sensitivity coefficients must also be calculated numerically. This is accomplished using a finite difference technique whereby we perturb a single dependent variable in Eq. (14) by a small amount ε , re-compute the new perturbed regression coefficients via the least squares method, subtract the new coefficient $\hat{a}_{q,0}$ from the unperturbed value $a_{q,0}$, and divide the quantity by ε [15]. The complete set of sensitivity coefficients are determined by repeating this procedure for each one of the dependent variables.

Non-Propagated Uncertainty

The non-propagated uncertainty is given by

$$u_{np}(a_{q,0}) = \sqrt{\frac{\sigma_{FIT}^2}{3} + \sigma_{RES}^2 \sum_{n=1}^N \left(\frac{\partial a_{q,0}}{\partial \Gamma_{q,n}} \right)^2} \quad (15A)$$

where $\sigma_{FIT}/\sqrt{3}$ is the standard deviation of the mean of 3 values of $a_{q,0}$ calculated using 2nd, 3rd, and 4th degree polynomial fits. This uncertainty accounts for the fact that there is no physical basis to select the degree of the polynomial to use. The second term is the “so called” classical solution for the uncertainty of the y-intercept [14]. It is calculated by multiplying the sensitivity coefficient by the standard deviation of the curve fit residuals or also known as the standard error of regression (σ_{RES}), which is calculated by [16]

$$\sigma_{RES} = \sqrt{\frac{1}{N-2} \sum_{n=1}^N \left(\Gamma_{q,FIT}(\Delta P_{23_n}) - \Gamma_{q,n} \right)^2}. \quad (15B)$$

The second term accounts for the uncertainty of the curve fit, but does not include systematic uncertainties attributed to the zero-pressure offset, calibration of the pressure sensors, etc. These uncertainties are accounted for in the propagated uncertainty.

Propagated Uncertainty

Measurement errors in $\Delta P_{23,n}$ and in $\Gamma_{q,n}$ propagate through Eq. (14) and lead to the following expression for propagated uncertainty,

$$\begin{aligned}
u_p^2(a_{q,0}) = & \sum_{n=1}^N \left(\frac{\partial a_{q,0}}{\partial \Delta P_{23,n}} \right)^2 u^2(\Delta P_{23,n}) \\
& + \sum_{m=1}^N \sum_{n=1}^N (1 - \delta_{mn}) \left(\frac{\partial a_{q,0}}{\partial \Delta P_{23,m}} \right) \left(\frac{\partial a_{q,0}}{\partial \Delta P_{23,n}} \right) r(\Delta P_{23,m}, \Delta P_{23,n}) u(\Delta P_{23,m}) u(\Delta P_{23,n}) \\
& + \sum_{n=1}^N \left(\frac{\partial a_{q,0}}{\partial \Gamma_{q,n}} \right)^2 u^2(\Gamma_{q,n}) + \sum_{m=1}^N \sum_{n=1}^N (1 - \delta_{mn}) \left(\frac{\partial a_{q,0}}{\partial \Gamma_{q,m}} \right) \left(\frac{\partial a_{q,0}}{\partial \Gamma_{q,n}} \right) r(\Gamma_{q,m}, \Gamma_{q,n}) u(\Gamma_{q,m}) u(\Gamma_{q,n}) \\
& + \sum_{m=1}^N \sum_{n=1}^N (1 - \delta_{mn}) \left(\frac{\partial a_{q,0}}{\partial \Delta P_{23,m}} \right) \left(\frac{\partial a_{q,0}}{\partial \Gamma_{q,n}} \right) r(\Delta P_{23,m}, \Gamma_{q,n}) u(\Delta P_{23,m}) u(\Gamma_{q,n})
\end{aligned} \tag{16A}$$

Generally speaking, the input variables are correlated so that the correlation coefficients $r(\Delta P_{23,m}, \Delta P_{23,n})$, $r(\Gamma_{q,m}, \Gamma_{q,n})$, and $r(\Delta P_{23,m}, \Gamma_{q,n})$ are not zero, but have some intermediate value between 0 and 1. We estimate the values of the correlation coefficient using an approach similar to Coleman [14]. Each correlation coefficient and its corresponding uncertainties are decomposed into their elementary or base uncertainty sources. Elemental uncertainty sources include: 1) the calibration uncertainty of the pressure transducers, $u(\Delta P_{\text{cal}})$; 2) the zero-drift of pressure transducers, $u(\Delta P_{\text{zero}})$; and 3) the uncertainty of yaw angle alignment, $u(\theta)$. The elemental uncertainty sources have cross-correlation coefficients that are equal to zero; however, the elemental uncertainty sources may or may not be correlated with themselves. For example, since all the transducers are calibrated by the same pressure standard the calibration uncertainty is taken to be perfectly correlated when the sensors are used to measure the same nominal pressure. Thus, at the yaw-null pressure condition of $\Delta P_{23} = 0$, the calibration uncertainties of the two pressure transducers that measure ΔP_{12} and ΔP_{13} are perfectly correlated, and the correlation coefficient is unity, $r(\Delta P_{13,\text{cal}}, \Delta P_{12,\text{cal}}) = 1$. On the other hand, the calibration uncertainties are taken to be uncorrelated and have correlation coefficient equal to zero for the same transducer (or different transducers) used to measure different pressures. In cases where it is unclear whether an elemental correlation coefficient should be 0 or 1, we conservatively use the value that results in the larger uncertainty. By associating the perfectly correlated elemental uncertainties with Eq. (12B) and uncorrelated uncertainties with Eq. (12C) we simplify the propagated uncertainty in Eq. (16A) to

$$u_p(a_{q,0}) = \sqrt{\left[\sum_{n=1}^N \left(\frac{\partial a_{q,0}}{\partial \Delta P_{23,n}} \right) u(\Delta P_{23,n}) \right]^2 + \left[\sum_{n=1}^N \left(\frac{\partial a_{q,0}}{\partial \Gamma_{q,1,n}} \right) u(\Gamma_{q,1,n}) \right]^2 + \left[\sum_{n=1}^N \left(\frac{\partial a_{q,0}}{\partial \Gamma_{q,2,n}} \right) u(\Gamma_{q,2,n}) \right]^2} \tag{16B}$$

where the term $u(\Delta P_{23,n})$ is the uncertainty in the yaw pressure measurement given in Eq. (4B), and $u(\Gamma_{q,1,n})$ and $u(\Gamma_{q,2,n})$ are the uncertainties of the generic probe parameters given by

$$u(\Gamma_{q,1,n}) = \begin{cases} u(\theta) & q=1 \\ \sqrt{2}u(\Delta P_{\text{cal}}) & q=2, \\ u(\Delta P_{\text{cal}}) & q=3 \end{cases} \tag{16C}$$

and

$$u(\Gamma_{q,2,n}) = \begin{cases} 0 & q=1 \\ \sqrt{2}u(\Delta P_{\text{zero}}) & q=2, \\ u(\Delta P_{\text{zero}}) & q=3 \end{cases} \quad (16D)$$

respectively. The use of this approximate method is justified since it yields a conservative estimate of the uncertainty, and $u_p(a_{q,0})$ is not the dominate source of uncertainty in the uncertainty budget.

Combined Uncertainty

The combined uncertainty, including both propagated and non-propagated components is

$$u_c(a_{q,0}) = \sqrt{\frac{\sigma_{\text{FIT}}^2}{3} + \sigma_{\text{RES}}^2 \sum_{n=1}^N \left(\frac{\partial a_{q,0}}{\partial \Gamma_{q,n}} \right)^2 + \left[\sum_{n=1}^N \left(\frac{\partial a_{q,0}}{\partial \Delta P_{23n}} \right) u(\Delta P_{23n}) \right]^2 + \left[\sum_{n=1}^N \left(\frac{\partial a_{q,0}}{\partial \Gamma_{q,n}} \right) u(\Gamma_{q,1,n}) \right]^2 + \left[\sum_{n=1}^N \left(\frac{\partial a_{q,0}}{\partial \Gamma_{q,n}} \right) u(\Gamma_{q,2,n}) \right]^2}. \quad (17)$$

5.3 Uncertainty Analysis of F_1 and F_2 .

The uncertainty of the calibration factors F_1 and F_2 in Eqs. (6A) and (6B) are determined using Eq. (12B). The expression for the expanded uncertainty expression of F_1 is

$$U(F_1) = 2 \sqrt{\frac{u^2(\Delta P_{45,\text{NULL}})}{\Delta P_{12,\text{NULL}}^2} + \frac{u^2(\Delta P_{12,\text{NULL}}) F_1^2}{\Delta P_{12,\text{NULL}}^2} + u_{\text{reprd}}^2(F_1)} \quad (18A)$$

where $u(\Delta P_{45,\text{NULL}})$ and $u(\Delta P_{12,\text{NULL}})$ are the uncertainties of the null parameters specified in Eq. (17) for $q = 2$ and 3 , respectively. The values of the null parameters are determined using the CFM from Section 4.2. Also, $u_{\text{reprd}}(F_1)$ is the standard reproducibility uncertainty documented in Section 4.5.

The expression for the expanded uncertainty for F_2 is

$$U_r(F_2) = 2 \sqrt{\frac{u_r^2(\rho)}{4} + u_r^2(V_{\text{LDA}}) + \frac{u_r^2(\Delta P_{12,\text{NULL}})}{4} + u_{\text{reprd}}^2(F_2)} \quad (18B)$$

where $u_r(V_{\text{LDA}})$ is the relative standard uncertainty of the LDA specified in Section 2, $u_r(\rho)$ is the relative standard uncertainty in density specified in Section 2, and $u_{\text{reprd}}(F_2)$ is the relative standard uncertainty attributed to reproducibility specified in Section 4.5

The expanded uncertainties of F_1 and F_2 are plotted in Figs. 7E and 7F for the spherical probe and in Figs. 8E and 8F for the prism probe. The expanded uncertainty of F_2 was comparable for both probes for $\alpha = -20$ to 20 . The prism probe exhibited an uncertainty ranging from 0.9 % to 1.25 % depending on airspeed while the uncertainty of the spherical probe ranges from 0.9 % to 1.1 %. The largest uncertainty sources for both probes include the reproducibility of repeated calibrations and the LDA airspeed standard, which together, contributed between 60 % and 80 % in all cases.

6 LIMITATIONS OF METHOD 2F CAN CAUSE LARGE UNCERTAINTIES IN FIELD MEASUREMENTS

We identified two limitations of Method 2F that can result in large biases when 3-D probes are used in field measurements. First, Method 2F does not adequately account for the Re -dependence of probe calibration factors; instead Method 2F approximates F_1 and F_2 as a function of α only.¹¹ This approach is reasonable for the spherical probe for pitch angles $-20 \leq \alpha \leq 20$ since $F_{2,SPHERICAL}$ is nearly independent of Reynolds number (or air speed). In contrast, $F_{2,PRISM}$ strongly depends on Reynolds number, especially at the lower air speeds < 10 m/s. If we had calibrated the prism probe using Method 2F and then used the probe in the field, we would over-report low velocity (5 m/s) measurements by nearly 6%. Therefore, to obtain accurate low velocities measurements in field applications, a prism probe must be calibrated over the range of velocities it will be used.

Second, more stringent uncertainty requirements are needed for the yaw-null pressure measurement at low air speeds (< 10 m/s). Method 2F specifies the yaw pressure transducer should have full-scale range of ± 124.5 Pa and an expanded uncertainty of 2.5 Pa (1% of full-scale). In addition, during stack application, the protocol allows the yaw pressure transducer to have a zero drift as large as 7.5 Pa. If these specifications are met, the uncertainty in yaw pressure $u(\Delta P_{yaw})$ will significantly increase the measurement uncertainty at low flue gas velocities.

Even if $u(\Delta P_{yaw})$ is negligible, a third uncertainty source, not considered in Method 2F, should be considered. This uncertainty $u(\Delta P_{23 \neq 0})$ occurs when the null parameters (θ_{NULL} , $\Delta P_{45, NULL}$, and $\Delta P_{12, NULL}$) are measured at a non-zero yaw-pressure $\Delta P_{23} \neq 0$. In practice, noisy pressure signals (especially during in-stack applications) make it difficult to find the exact yaw-null angle where $\Delta P_{23} = 0$. Consequently, the null parameters are generally measured at pressures slightly offset from zero, thereby increasing the uncertainty.

Accounting for all three uncertainty sources, the total yaw-pressure uncertainty is

$$u(P_{offset}) = \sqrt{u^2(\Delta P_{cal}) + u^2(\Delta P_{zero}) + u^2(\Delta P_{23 \neq 0})} \quad (19)$$

where $u(\Delta P_{cal})$ is the uncertainty of the yaw pressure transducer, $u(\Delta P_{zero})$ is the uncertainty of the zero-drift during a measurement, and $u(\Delta P_{23 \neq 0}) = \Delta P_{23} / \sqrt{3}$ is the uncertainty in yaw-pressure because it is slightly offset from zero, $\Delta P_{23} \neq 0$. We take the latter uncertainty to have rectangular distribution so that ΔP_{23} is multiplied by the factor $1/3^{1/2}$ [12].

We emphasize that the Method 2F allowable-yaw-pressure, zero-offset uncertainty will be a significant contributor to the overall uncertainty budget at low flows because $u(P_{offset})$ will be a significant fraction of the dynamic pressure.

In our current work, $u(P_{offset})$ is negligible relative to other uncertainty sources. First, we used the CFM introduced in Section 4.2 to ensure that the null parameters are determined at exactly

¹¹ Method 2F requires that the calibration factors are measured over a range of pitch angles, but at each pitch angle F_1 and F_2 are only measured at 2 air speeds consisting of 18.3 m/s and 27.4 m/s. The average F_1 and F_2 at these 2 air speeds are curve fit as a function of α , and the calibration curve fits are extrapolated to lower flue gas velocities in stack applications [5].

$\Delta P_{23} = 0$. Second, we used differential pressure transducers (described in Section 3.1) with a small zero-drift uncertainty relative to the dynamic pressure of the air stream specified in Eq. (1). At the lowest velocity setting of $V_{LDA} = 5$ m/s the dynamic pressure is $\Delta P_{dyn} = 15$ Pa so that $u(\Delta P_{offset}) / \Delta P_{LDA} < 0.001$. In contrast, Method 2F specifications for the uncertainty of yaw pressure measurement are not as stringent, allowing the calibration uncertainty to be as large as 2.5 Pa and the zero drift as large as 7.5 Pa [5]. In this case, at 5 m/s the yaw-pressure uncertainty normalized by the dynamic pressure is significant, $u(\Delta P_{offset}) / \Delta P_{dyn} = 0.53$.

To estimate how the uncertainty in the yaw-pressure measurement affects the yaw-null angle and the calibration factors, we conservatively specified $u(P_{offset}) = 2.5$ Pa and calculated the uncertainties $u(\theta_{NULL})$, $u(F_1)$ and $u(F_2)$ at different air speeds. The expanded uncertainty attributed *solely* to the zero-offset effect is given by

$$U(I_{q,offset}) = 2 \left| \frac{\partial I_{q,FIT}}{\partial \Delta P_{23}} \right|_{NULL} u(P_{offset}) = 2 |a_{q,1}| u(P_{offset}) \quad (20)$$

where I_q is the generic probe variable in Table 3, $U(I_{q,offset})$ compactly represents the expanded uncertainties: $U(\theta_{NULL,offset})$, $U(F_{1,offset})$, and $U(F_{2,offset})$ for $q = 1, 4$, and 5 , respectively. The term $[\partial I_{q,FIT} / \partial \Delta P_{23}]_{NULL}$ is the slope of the curve fit specified in Eq. (7). The slope is evaluated at the null condition where $\Delta P_{23} = 0$, and therefore equals the fit coefficient $a_{q,1}$.

Figure 10 shows the expanded uncertainties $U(\theta_{NULL,offset})$, $U(F_{1,offset})$, and $U(F_{2,offset})$ plotted versus the pitch angle (α) for $u(P_{offset}) = 2.5$ Pa. As denoted by the legend at the top of the figure, each symbol corresponds to a constant airspeed between 5 m/s and 30 m/s. Results for the spherical probe (left) and the prism probe (right) are plotted on the same x and y scale so that they can be easily compared. Results for the prism probe and spherical probe are nearly identical at all airspeeds, except for $U(F_{1,offset})$ at the lowest airspeed. The dependence on pitch is small, but, in general the uncertainty slightly increases at large negative or positive pitch angles. As expected, the largest uncertainties occur at the lowest airspeed of 5 m/s where the dynamic pressure is a larger fraction of $u(P_{offset})$. The uncertainty in $U(\theta_{NULL,offset})$ and $U(F_{2,offset})$ are substantial at 5 m/s, approximately 5° and 10% , respectively for pitch angles ranging from $\alpha = -20$ to 20 . The uncertainties are lower at 10 m/s, but still are significant being approximately 1.5° and 1.5% , respectively.

These results suggest that zero-offset effects can make a significant contribution to the uncertainty budget in field applications at airspeeds at or below 10 m/s. To improve the uncertainty requires more accurate yaw-pressure transducers and ensuring that the null parameters are measured at $\Delta P_{23} = 0$.

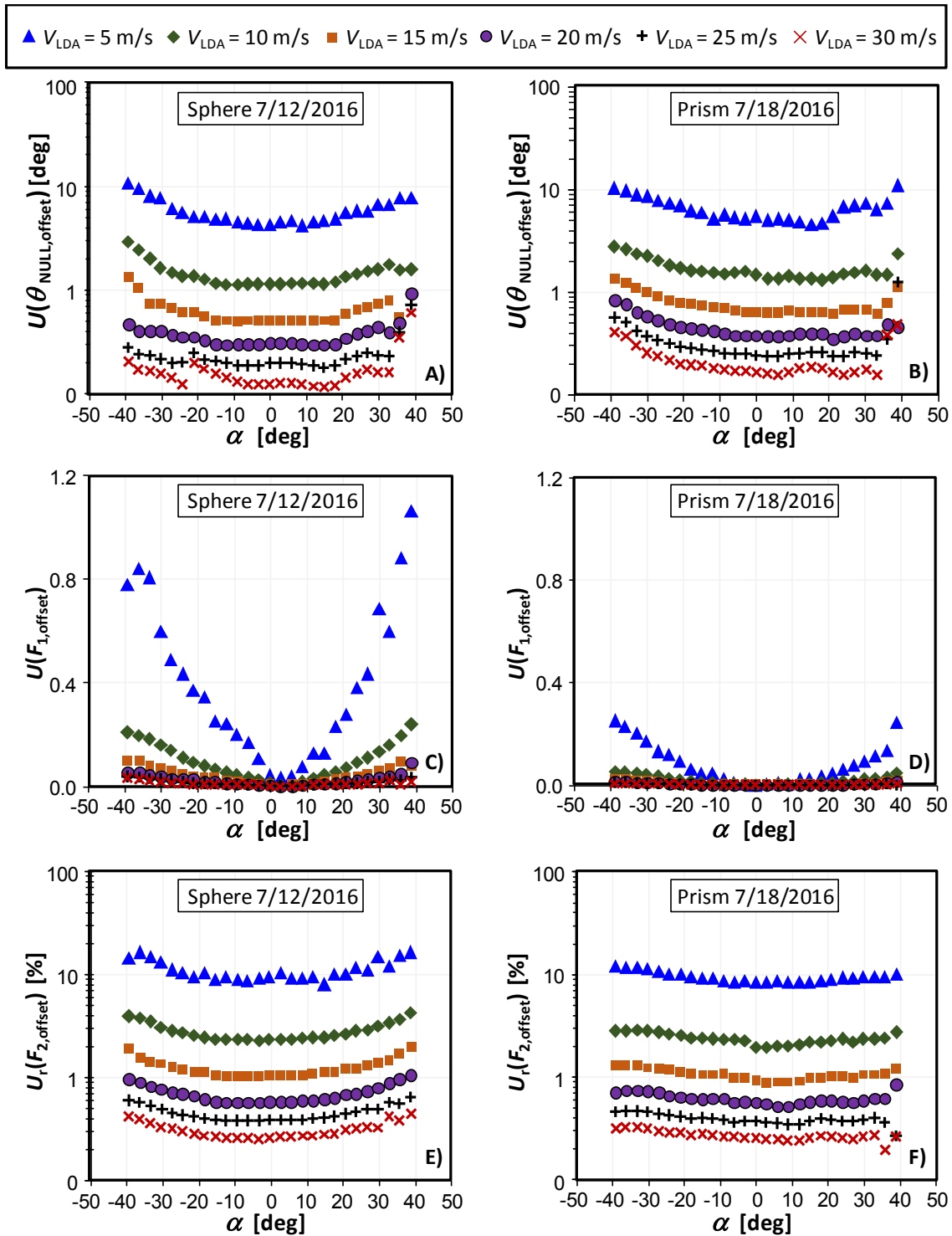


Figure 10. The expanded uncertainties in θ_{NULL} , F_1 , and F_2 attributed an uncertainty in the zero-offset pressure $u(P_{offset}) = 2.5$ Pa for the spherical probe (left) and prism probe (right) for airspeeds from 5 m/s to 30 m/s and pitch angles from -40 to 40 .

7 DISCUSSION

We calibrated a spherical probe and prism probe using a yaw-nulling method for pitch angles $-45 \leq \alpha \leq 45$ and air speeds $5 \text{ m/s} \leq V_{\text{LDA}} \leq 30 \text{ m/s}$. Here, we focus on the narrower range $-20 \leq \alpha \leq 20$ which includes the conditions encountered in most industrial smokestacks. We determined the pitch calibration factor F_1 and the velocity calibration factor F_2 over the range of calibration conditions. Three repeated calibrations of the spherical probe and two repeated calibrations of the prism probe were mutually consistent within $\pm 0.75\%$ of F_2 . The dependence of F_2 on the Reynolds number (Re) differed significantly between the two probes. For the spherical probe, F_2 was nearly Re -independent (deviations from the mean were less than $\pm 1\%$) except at the lowest air speed of 5 m/s, where deviations increased to nearly 2%. In contrast, F_2 for the prism probe had a strong Re -dependence and the deviations from the mean were as large as 6%. *Based on this result, the prism probe should be calibrated over the range of airspeeds for which it will be used to achieve accuracies better than 6%.*

To apply the NIST calibration results to flue gas measurements in the field, we developed a calibration curve that determines α and F_2 from measurements of the pitch pressure and velocity pressure at the null condition. This calibration curve accounts for the Re -dependence of the prism probe. In contrast, EPA's protocol 2F, which is widely used for stack measurements, does not account for Re effects. If method 2F is implemented using the prism probe calibrated herein, velocity errors exceeding 5% could occur. The NIST calibration curve accounts for the Re -dependence of the prism probe and is accurate to better than 1% for airspeeds in the range $5 \text{ m/s} \leq V \leq 30 \text{ m/s}$ and pitch angles from -20 to 20 .

We determined the yaw-null angle θ_{NULL} and the null pitch pressure $\Delta P_{45,\text{NULL}}$ and the null velocity pressure $\Delta P_{12,\text{NULL}}$ using a *Curve Fit Method*. We rotated the probe about its axis and measured yaw angles θ , pitch pressures ΔP_{45} , velocity pressures ΔP_{12} , and yaw pressures ΔP_{23} for values of ΔP_{23} surrounding the null condition $\Delta P_{23} = 0$. We fitted polynomial curves to three sets of data pairs: $(\Delta P_{23}, \theta)$; $(\Delta P_{23}, \Delta P_{45})$; and $(\Delta P_{23}, \Delta P_{12})$. Then, we determined θ_{NULL} , $\Delta P_{45,\text{NULL}}$, and $\Delta P_{12,\text{NULL}}$ by evaluating the fitted curves at $\Delta P_{23} = 0$. This procedure avoids errors resulting from zero-offsets of pressure transducers, which often occur in field applications when the null conditions are measured at non-zero yaw pressures. To estimate the size of zero-offset effects, we multiplied the EPA's yaw pressure specification (2.5 Pa) for stack emission flow measurements by the slope of the fitted curves. The zero-offset effects increase significantly at lower airspeeds. At 5 m/s the zero-offset for the spherical probe is 10%; for the prism probe, it ranges from 8.5% to 10%, depending on the pitch angle. At 10 m/s the zero-offset was 2.5% for the spherical probe and 2% for the prism probe.

The expanded percentage uncertainty at a 95% confidence level of F_2 was comparable for both probes. For the prism probe, $U(F_2)$ ranged from 0.9% to 1.25% depending on airspeed; for the spherical probe, $U(F_2)$ ranged from 0.9% to 1.1%. For both probes the largest uncertainty source was the reproducibility of repeated calibrations and the LDA standard; together, they contributed 60% to 80% of $U(F_2)$.

8 REFERENCES

-
- [1] Shinder, I. I., Khromchenko, V. B., and Moldover, M. R., ***NIST's New 3D Airspeed Calibration Rig, Addresses Turbulent Flow Measurement Challenges***, 9th International Symposium on Fluid Flow Measurement (ISFFM), Washington, DC, U. S., April 2015.

-
- [2] Norfleet, S. K., Muzio L. J., and Martz T. D., ***An Examination of Bias in Method 2 Measurements Under Controlled Non-Axial Flow Conditions***, Report by RMB Consulting and Research, Inc., May 22, 1998.
- [3] Borthwick, R., and Bundy, M., ***Quantification of a precision point source for generating carbon dioxide emissions***, EPRI CEM User Group Conference and Exhibit, Chicago, IL, June 8, 2011.
- [4] Quick, J. C., ***Carbon dioxide emission tallies for 210 U.S. coal-fired power plants: A comparison of two accounting methods***, Journal of the Air & Waste Management Association, January 2014.
- [5] Environmental Protection Agency, 40 CFR Part 60 ***Application Method 2F Stack Gas-Velocity/Volumetric Flow Rate-3D probe***, Washington D.C., 1996.
- [6] Shinder, I. I., Crowley, C. J., Filla, B. J., Moldover, M. R., ***Improvements to NIST's Air Speed Calibration Service***, Flow Measurement and Instrumentation, Vol. 44, pp. 19–26, 2015.
- [7] Yeh, T. T., Hall, J. M., ***An Uncertainty Analysis of the NIST Airspeed Standards***, ASME Paper FEDSM2007-37560, ASME/JSME 5th Joint Fluids Engineering Conference, pp. 135-142, San Diego, California, USA, 2007.
- [8] Yeh, T. T. and Hall, J. M. ***Uncertainty of NIST Airspeed Calibrations***, Technical document of Fluid Flow Group, NIST, Gaithersburg, Maryland, USA, 2008.
- [9] Yeh, T. T., Hall, J. M., ***Air Speed Calibration Service***, NIST Special Publication 250-79, National Institute of Standards and Technology, Gaithersburg, Maryland, 2006.
- [10] Shinder, I. I., Crowley, C. J., Filla, B. J., Moldover, M. R., ***Improvements to NIST's Air Speed Calibration Service***, 16th International Flow Measurement Conference, Flomeko 2013, Paris, France September 24-26, 2013.
- [11] Jaeger, K. B. and Davis, R. S. ***A Primer for Mass Metrology***, National Bureau of Standards (U.S.), Special Publication 700-1, Industrial Measurement Series. 1987: 79.
- [12] Taylor, B. N. and Kuyatt, C. E., ***Guidelines for Evaluating and Expressing the Uncertainty of NIST Measurement Results***, NIST Technical Note 1297, National Institute of Standards and Technology, January 1993.
- [13] International Organization for Standardization, ***Guide to the Expression of Uncertainty in Measurement***, Switzerland, 1996 edition.
- [14] Coleman, H. W. and Steele, W. G., ***Experimentation and Uncertainty Analysis for Engineers***, 3rd ed., John Wiley and Sons, Inc., N.Y., 2009.
- [15] DuChateau, P. and Zachmann, D., ***Applied Partial Differential Equations***, Harper and Row Publishers Inc., New York, N.Y., 1989.
- [16] Kennedy, John B. and Adam M. Neville, ***Basic Statistical Methods for Engineers and Scientists***, 3rd ed., Harper and Row, 1986.